

## NRC Publications Archive Archives des publications du CNRC

### First light and reionisation epoch simulations (FLARES). IV. The size evolution of galaxies at $z \geq 5$

Roper, William J.; Lovell, Christopher C.; Vijayan, Aswin P.; Marshall, Madeline A.; Irodotou, Dimitrios; Kuusisto, Jussi K.; Thomas, Peter A.; Wilkins, Stephen M.

This publication could be one of several versions: author's original, accepted manuscript or the publisher's version. / La version de cette publication peut être l'une des suivantes : la version prépublication de l'auteur, la version acceptée du manuscrit ou la version de l'éditeur.

For the publisher's version, please access the DOI link below. / Pour consulter la version de l'éditeur, utilisez le lien DOI ci-dessous.

#### **Publisher's version / Version de l'éditeur:**

<https://doi.org/10.1093/mnras/stac1368>

*Monthly Notices of the Royal Astronomical Society*, 514, 2, pp. 1921-1939, 2022-05-19

#### **NRC Publications Archive Record / Notice des Archives des publications du CNRC :**

<https://nrc-publications.canada.ca/eng/view/object/?id=e9dcc5d6-3295-4b56-b925-dc5bf883656c>

<https://publications-cnrc.canada.ca/fra/voir/objet/?id=e9dcc5d6-3295-4b56-b925-dc5bf883656c>

Access and use of this website and the material on it are subject to the Terms and Conditions set forth at

<https://nrc-publications.canada.ca/eng/copyright>

READ THESE TERMS AND CONDITIONS CAREFULLY BEFORE USING THIS WEBSITE.

L'accès à ce site Web et l'utilisation de son contenu sont assujettis aux conditions présentées dans le site

<https://publications-cnrc.canada.ca/fra/droits>







LISEZ CES CONDITIONS ATTENTIVEMENT AVANT D'UTILISER CE SITE WEB.

**Questions?** Contact the NRC Publications Archive team at

PublicationsArchive-ArchivesPublications@nrc-cnrc.gc.ca. If you wish to email the authors directly, please see the first page of the publication for their contact information.

**Vous avez des questions?** Nous pouvons vous aider. Pour communiquer directement avec un auteur, consultez la première page de la revue dans laquelle son article a été publié afin de trouver ses coordonnées. Si vous n'arrivez pas à les repérer, communiquez avec nous à PublicationsArchive-ArchivesPublications@nrc-cnrc.gc.ca.

# First Light And Reionisation Epoch Simulations (FLARES) – IV. The size evolution of galaxies at $z \geq 5$

William J. Roper <sup>1</sup>,<sup>\*</sup> Christopher C. Lovell <sup>1,2</sup> Aswin P. Vijayan <sup>1,3,4</sup> Madeline A. Marshall,<sup>5,6</sup> Dimitrios Irodotou <sup>1,7</sup> Jussi K. Kuusisto,<sup>1</sup> Peter A. Thomas <sup>1</sup> and Stephen M. Wilkins <sup>1</sup>

<sup>1</sup>*Astronomy Centre, University of Sussex, Falmer, Brighton BN1 9QH, UK*

<sup>2</sup>*Centre for Astrophysics Research, School of Physics, Astronomy and Mathematics, University of Hertfordshire, Hatfield AL10 9AB, UK*

<sup>3</sup>*Cosmic Dawn Center (DAWN), Rådmandsgade 62, DK-2200 København N, Denmark*

<sup>4</sup>*DTU Space, Technical University of Denmark, Elektrovej 327, DK-2800 Kongens Lyngby, Denmark*

<sup>5</sup>*National Research Council of Canada, Herzberg Astronomy and Astrophysics Research Centre, 5071 West Saanich Road, Victoria, BC V9E 2E7, Canada*

<sup>6</sup>*ARC Centre of Excellence for All Sky Astrophysics in 3 Dimensions (ASTRO 3D), Stromlo, ACT 2611, Australia*

<sup>7</sup>*Department of Physics, University of Helsinki, Gustaf Hällströmin katu 2, FI-00014 Helsinki, Finland*

Accepted 2022 May 12. Received 2022 May 3; in original form 2022 March 25

## ABSTRACT

We present the intrinsic and observed sizes of galaxies at  $z \geq 5$  in the First Light And Reionisation Epoch Simulations (FLARES). We employ the large effective volume of FLARES to produce a sizeable sample of high-redshift galaxies with intrinsic and observed luminosities and half-light radii in a range of rest-frame ultraviolet (UV) and visual photometric bands. This sample contains a significant number of intrinsically ultracompact galaxies in the far-UV (1500 Å), leading to a negative intrinsic far-UV size–luminosity relation. However, after the inclusion of the effects of dust these same compact galaxies exhibit observed sizes that are as much as 50 times larger than those measured from the intrinsic emission, and broadly agree with a range of observational samples. This increase in size is driven by the concentration of dust in the core of galaxies, heavily attenuating the intrinsically brightest regions. At fixed luminosity we find a galaxy size redshift evolution with a slope of  $m = 1.21\text{--}1.87$  depending on the luminosity sample in question, and we demonstrate the wavelength dependence of the size–luminosity relation that will soon be probed by the *James Webb Space Telescope*.

**Key words:** galaxies: evolution – galaxies: high-redshift – galaxies: photometry.

## 1 INTRODUCTION

Galaxy sizes are governed by a range of processes including galaxy mergers, instabilities, gas accretion, gas transport, star formation, and feedback (Conselice 2014). Studying galaxy sizes helps us to understand the interplay between these key astrophysical processes and galactic structure. By extension, understanding how galaxy sizes evolve tells us how these fundamental physical mechanisms, and the interplay between them, change over time.

At fixed redshift, the size–luminosity relation can be expressed as a power law of the form

$$R = R_0 \left( \frac{L}{L_{z=3}^*} \right)^\beta, \quad (1)$$

where  $R_0$  is a normalization factor,  $\beta$  is the slope of the size–luminosity relation, and  $L_{z=3}^*$  is the characteristic ultraviolet (UV) luminosity for  $z \sim 3$  Lyman-break galaxies (with value  $L_{z=3}^* = 10^{29.03} \text{ erg s}^{-1} \text{ Hz}^{-1}$ ), which corresponds to  $M_{1600} = -21.0$  (Steidel et al. 1999). As a function of redshift the size evolution can be expressed as

$$R(z) = R_{0,z=0} (1+z)^{-m}, \quad (2)$$

where  $R_{0,z=0}$  is another normalization factor corresponding to the size of a galaxy at  $z = 0$  and  $m$  is the slope of the redshift evolution. In addition to its importance to understanding physical processes, probes of the size–luminosity relation and its evolution are indispensable to our understanding of survey completeness and by extension the luminosity function (Kawamata et al. 2018; Bouwens et al. 2022).

In observations at low redshifts ( $z < 3$ ), galaxies have sizes of the order 1–30 proper kpc (pkpc), with actively star-forming galaxies typically larger than their quiescent counterparts (Zhang & Yang 2019; Kawinwanichakij et al. 2021). These galaxies exhibit a positive size–luminosity relation (van der Wel et al. 2014; Suess et al. 2019; Kawinwanichakij et al. 2021), although van der Wel et al. (2014) find a significant number density of compact and massive ( $R < 2$  pkpc,  $M/M_\odot > 10^{11}$ ) galaxies at  $z = 1.5\text{--}3$ , whose number density drops drastically by the current day.

The landscape is different at high redshift where we are primarily probing star-forming galaxies. A number of studies using deep *Hubble Space Telescope* (HST) fields have measured the sizes of  $z = 6\text{--}12$  Lyman-break galaxies (Oesch et al. 2010; Grazian et al. 2012; Mosleh et al. 2012; Huang et al. 2013; Ono et al. 2013; Holwerda et al. 2015, 2020; Kawamata et al. 2015, 2018; Shibuya, Ouchi & Harikane 2015). In contrast to the low-redshift size regime, these studies found bright star-forming galaxies with compact half-light radii of 0.5–1.0 pkpc.

\* E-mail: w.roper@sussex.ac.uk

There is a growing consensus that the high-redshift size–luminosity relation is positively sloped ( $\beta > 0$ ), as it is at low redshift, with a range of reported slopes and differing reports of  $\beta$ 's redshift evolution.

- (i) Grazian et al. (2012) find  $\beta = 0.3\text{--}0.5$  at  $z \sim 7$ .
- (ii) Huang et al. (2013) find  $\beta = [0.22, 0.25]$  for  $z = 4$  and  $z = 5$ , respectively.
- (iii) Holwerda et al. (2015) find  $\beta = 0.24 \pm 0.06$  at  $z \sim 7$  and  $\beta = 0.12 \pm 0.09$  at  $z \sim 9\text{--}10$ .
- (iv) Shibuya et al. (2015) find a redshift-independent slope of  $\beta = 0.27 \pm 0.01$  in the range  $z = 0\text{--}8$ .
- (v) Kawamata et al. (2018) find steeply sloped relations with  $\beta = [0.46, 0.46, 0.38, 0.56]$  at  $z = [6, 7, 8, 9]$ , respectively.

Recent lensing studies agree with the steeper slope of Kawamata et al. (2018), itself using a sample including lensed sources. Bouwens et al. (2022) find  $\beta = 0.40 \pm 0.04$  for a galaxy sample in the redshift range  $z \sim 6\text{--}8$ , while Yang et al. (2022) find  $\beta = 0.48 \pm 0.08$  for  $z \sim 6\text{--}7$  and  $\beta = 0.68 \pm 0.14$  for  $z \sim 8.5$  (assuming the Bradac lens model; Bradač et al. 2005). This steeper slope is driven by compact dim galaxies that are better sampled in lensing studies. Neufeld et al. (2021) also find extremely compact lensed galaxies with  $R_{1/2} < 200$  ppc in the Reionization Lensing Cluster Survey (RELICS) data set; they identify these galaxies as potential Lyman continuum (LyC) leakers, possibly representing a large contribution to reionization.

A similar range of results exists within measurements of the redshift dependence of galaxy size at fixed luminosity with slopes in the range  $1 < m < 1.5$  (Bouwens et al. 2004; Oesch et al. 2010; Ono et al. 2013; Kawamata et al. 2015, 2018; Shibuya et al. 2015; Laporte et al. 2016). This is consistent with two theoretical scenarios:  $m = 1$ , the expected scaling for systems of fixed mass (e.g. Bouwens et al. 2004), and  $m = 1.5$ , the expected evolution for systems with fixed circular velocity (e.g. Ferguson et al. 2004; Hathi, Malhotra & Rhoads 2008). However, galaxy sizes are not wholly dependent on these theoretical scalings with significant contributions from baryonic processes such as stellar and active galactic nuclei (AGN) feedback (Wyithe & Loeb 2011).

Simulations provide detailed information on the properties of the underlying components that make up galaxies. From this information we can probe large samples of galaxies with knowledge of the intrinsic physical processes governing their evolution, albeit processes that are themselves dictated by subgrid models that are sensitive to their physical model and parameter assumptions. The intrinsic properties of particles and their spatial distribution can be utilized to measure galaxy properties such as their half-mass/light radii at the mass resolution of the simulation without the associated uncertainties inherent in measurements of this kind in observations. Using this fidelity, the size–mass and size–luminosity relations have been probed by many simulations. However, much of this analysis still focuses on comparatively low redshifts. Furlong et al. (2017) analysed the EAGLE simulation and found a good agreement with observed trends using intrinsic particle measurements to find a positive ( $\beta > 0$ ) size–mass relation that flattens at  $z = 2$ , and an increase in size with decreasing redshift over the range  $z = 0\text{--}2$ .

At higher redshift ( $z = 6$ ), the SIMBA simulations (Davé et al. 2019) find a positive far-UV attenuated size–luminosity relation while showing the dust attenuated size is significantly larger than the intrinsic size, with the magnitude of this increase a function of stellar mass (Wu et al. 2020). This implies a flatter intrinsic size–luminosity relation at high redshift. This flattened intrinsic size–luminosity relation is particularly evident in the BLUETIDES simulation (Feng et al. 2016; Marshall et al. 2022), which has been used to probe the

UV and visual size–luminosity relations with synthetic observations at  $z \geq 7$ . In doing so they find a negative intrinsic size–luminosity relation ( $\beta < 0$ ) in the far-UV that flips to positive after the inclusion of dust attenuation ( $\beta > 0$ ). They also probe the redshift evolution of size, finding a shallow redshift evolution of  $m = 0.662 \pm 0.008$  in agreement with the redshift evolution of Holwerda et al. (2015). In addition to the higher redshift results derived from BLUETIDES, the ILLUSTRIS-TNG simulations have also exhibited a negative size–luminosity relation at  $z = 5$  (Popping et al. 2022).

The FIRE-2 simulations (Ma et al. 2018) present a sample of compact galaxies with sizes of  $0.05\text{--}1$  pkpc, in the range  $-22 < M_{\text{UV}} < -7$  at  $z = [6, 8, 10]$ . The sizes in this sample are measured from synthetic galaxy images of the intrinsic stellar emission using a non-parametric pixel method, which converts the pixel area containing half the total luminosity to a half-light radius. Unlike Marshall et al. (2022) this sample exhibits a size–mass relation and *B*-band size–luminosity relation with  $\beta > 0$ . The FIRE-2 galaxy sample extends to galaxies far fainter than those present in other simulated samples, which could explain the differences in size–mass and size–luminosity relations. They also present redshift evolution slopes derived in fixed stellar mass regimes that produce values of  $1 < m < 2$ , encompassing many of the observational measurements but extending to more extreme values for the brightest and most massive galaxies.

Clearly there is much work to be done in understanding galaxy size at this epoch, especially with the impending first light of the *James Webb Space Telescope* (JWST) and other next-generation observatories. In this paper, we analyse the large sample of galaxies produced by the First Light And Reionisation Epoch Simulations (FLARES) simulations (Lovell et al. 2021; Vijayan et al. 2021). FLARES is uniquely placed to complement previous studies of high-redshift galaxy size due to its enormous effective volume, coverage a wide array of environments during the Epoch of Reionization (EoR), and sufficient mass resolution, producing a large and robust galaxy sample. In previous work, we have shown that FLARES reproduces the distributions of stellar mass, star formation rate (SFR), and UV luminosity up to  $z = 10$ .

The rest of this paper is structured as follows. In Section 2, we detail the simulations themselves. In Section 3, we detail the methods used to make synthetic photometry and observations. In Section 4, we detail the galaxy sample and size measurement methods. In Section 5, we present the results of this analysis of the size–luminosity relation. We present our conclusions in Section 6. Throughout this work we assume a *Planck* Year 1 cosmology ( $\Omega_0 = 0.307$ ,  $\Omega_\Lambda = 0.693$ ,  $h = 0.6777$ ; Planck Collaboration I 2014) and a Chabrier stellar initial mass function (IMF; Chabrier 2003).

## 2 FIRST LIGHT AND REIONISATION EPOCH SIMULATIONS (FLARES)

FLARES is a simulation program targeting the EoR. It consists of 40 zoom simulations, targeting regions with a range of overdensities drawn from an enormous  $(3.2 \text{ comoving Gpc} - \text{cGpc})^3$  dark matter only simulation (Barnes et al. 2017a), which we will refer to as the ‘parent’. The regions are selected at  $z = 4.67$ , which ensures that extreme overdensities are only mildly non-linear, and thus the rank ordering of overdensities at higher redshifts is approximately preserved. Regions are defined as spheres with radius  $14 \text{ cMpc } h^{-1}$ , and their overdensities are selected to span a wide range ( $\delta = -0.479\text{--}0.970$ ; see table A1 of Lovell et al. 2021) in order to sample the most under- and overdense environments at this cosmic time, the latter containing a large sample of the most massive galaxies, thought to be biased to such regions (Chiang, Overzier & Gebhardt 2013; Lovell,

Thomas & Wilkins 2018). These regions are then resimulated with full hydrodynamics using the EAGLE model (Crain et al. 2015; Schaye et al. 2015).

The EAGLE project consists of a series of hydrodynamic cosmological simulations, with varying resolutions and box sizes. The code is based on a heavily modified version of P-GADGET-3, a smooth particle hydrodynamics (SPH) code last described in Springel et al. (2005b). The hydrodynamic solver is collectively known as ANARCHY (described in Schaller et al. 2015; Schaye et al. 2015), and adopts the pressure–entropy formulation described by Hopkins (2013), an artificial viscosity switch (Cullen & Dehnen 2010), and an artificial conduction switch (e.g. Price 2008). The model includes prescriptions for radiative cooling and photoheating (Wiersma, Schaye & Smith 2009a), star formation (Schaye & Dalla Vecchia 2008), stellar evolution and mass loss (Wiersma et al. 2009b), feedback from star formation (Dalla Vecchia & Schaye 2012), and black hole growth and AGN feedback (Springel, Di Matteo & Hernquist 2005a; Booth & Schaye 2009; Rosas-Guevara et al. 2015). The  $z = 0$  galaxy mass function, the mass–size relation for discs, and the gas mass–halo mass relation were used to calibrate the free parameters of the subgrid model. The model is in good agreement with a number of observables at low redshift not considered in the calibration (e.g. Furlong et al. 2015; Lagos et al. 2015; Trayford et al. 2015).

FLARES uses the AGNdT9 configuration of the model, which produces similar mass functions to the fiducial reference model, but better reproduces the hot gas properties of groups and clusters (Barnes et al. 2017b). It uses a higher value for  $C_{\text{visc}}$ , a parameter for the effective viscosity of the subgrid accretion, and a higher gas temperature increase from AGN feedback,  $\Delta T$ . These modifications give less frequent, more energetic AGN outbursts.

The FLARES simulations have an identical resolution to the 100 cMpc EAGLE reference simulation box, with a dark matter and an initial gas particle mass of  $m_{\text{dm}} = 9.7 \times 10^6 M_{\odot}$  and  $m_{\text{g}} = 1.8 \times 10^6 M_{\odot}$ , respectively, and has a gravitational softening length of 2.66 ckpc at  $z \geq 2.8$ .

In order to obtain a representative sample of the Universe, by combining these regions using appropriate weightings corresponding to their relative overdensity, we are able to create composite distribution functions that represent much larger volumes than those explicitly simulated. For a more detailed description of the simulation and weighting method we refer the reader to Lovell et al. (2021).

## 2.1 Galaxy extraction

We follow the same structure extraction method as the EAGLE project: this is explained in detail in McAlpine et al. (2016). In brief, dark matter overdensities are identified using a Friends-of-Friends (FoF) approach (Davis et al. 1985) with the usual linking length of  $\ell = 0.2\bar{x}$ , where  $\bar{x}$  is the mean interparticle separation. All other particle types are then assigned to the halo containing their nearest dark matter neighbour. These FoF haloes are then refined to produced self-bound ‘subgroups’ (galaxies) containing both dark matter and baryonic particles using the SUBFIND algorithm (Springel et al. 2001; Dolag et al. 2009).

The SUBFIND method involves finding saddle points in the density field in a FoF halo to identify self-bound substructures. This can lead to spurious oversplitting of extremely dense galaxies where saddle points are misidentified near density peaks. These objects often contain mainly a single particle type and have anomalous integrated properties. Although they make up  $< 0.1$  per cent of all galaxies  $> 10^8 M_{\odot}$  at  $z = 5$ , we identify and recombine them into their

parent structure in post-processing. To do this we label a ‘galaxy’ as spurious if it has any zero mass contributions in the stellar, gas, or dark matter components. We remove the spurious galaxies from the SUBFIND catalogue and add their particle properties to the parent ‘central’ subhalo, including the reassigned particles in any integrated quantities.

In a minority of pathological cases tidal stripping can cause galaxies to exhibit diffuse populations of particles at large radii. Although identified by SUBFIND as belonging to a galaxy, these distributions can have a large effect on integrated quantities such as the total luminosity and the half-light radius. For this reason we adopt a 30 pkpc aperture in line with all EAGLE and FLARES papers and calculate all integrated properties using only particles associated with each subgroup within this aperture. This aperture ensures the majority of galaxies have mass distributions that are wholly within this aperture and any erroneous distributions at large radii are omitted.

## 3 MODELLING PHOTOMETRY

We use the approach presented in Vijayan et al. (2021, (henceforth FLARES II) to produce resolved galaxy images, both including and excluding the effects of dust. We first produce spectral energy distributions (SEDs) and then apply top-hat rest-frame UV and visual band filters to extract photometry. As in FLARES II we focus on the stellar emission, deferring the treatment of accretion on to the supermassive black holes to a future work. However, as will be shown in the coming sections this simplification does not pose a significant challenge to the results of this work. This approach broadly follows Wilkins et al. (2016, 2017, 2018, 2020), with modifications to the dust treatment. For a full description of this method and discussion of the free parameters see FLARESII. What follows is a brief summary of the approach to compute galaxy images.

### 3.1 Spectral energy distribution modelling

In this work, we use the SYNTHOBS module<sup>1</sup> to produce synthetic rest-frame photometry primarily focusing on a top-hat far-UV (1500 Å) filter with a wavelength range of  $1300 \leq \lambda \leq 1700$  Å. We do however calculate results for a range of different filters all shown in the example SED in Fig. 1. Each component of the stellar luminosity can be included independently enabling the probing of both the intrinsic luminosity and the effects of dust extinction. In this section, we briefly detail each component.

#### 3.1.1 Stellar emission

For the pure stellar emission we start with a simple stellar population model (SSP) by associating each stellar particle with a stellar SED based on the particle’s age and metallicity. As with FLARES II we use v2.2.1 of the Binary Population and Spectral Synthesis (BPASS) stellar population synthesis (SPS) models (Stanway & Eldridge 2018) and assume a Chabrier (2003) IMF. As shown in Wilkins et al. (2016, 2017, 2018) the resulting luminosities are sensitive to the choice of SPS and IMF used in their derivation.

#### 3.1.2 Nebular emission

To account for the LyC emission of young stellar populations we associate young stellar particles ( $t < 10$  Myr, following the

<sup>1</sup>[github.com/stephenmwilkins/SynthObs](https://github.com/stephenmwilkins/SynthObs)

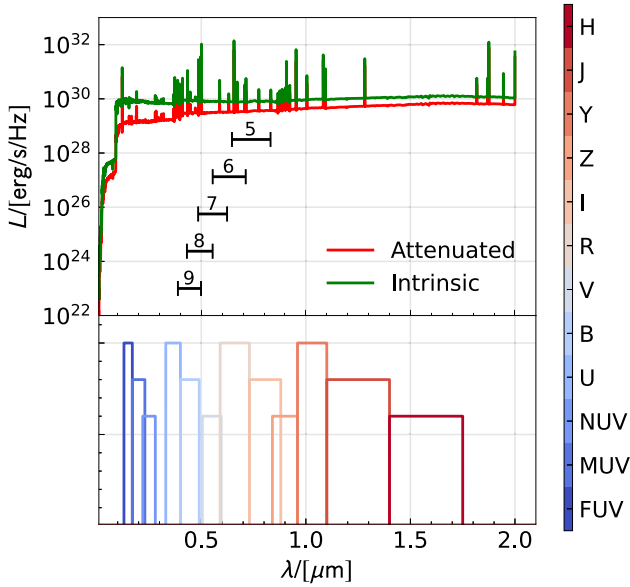


**Figure 1.** The median rest-frame SEDs for all galaxies in all FLARES regions at  $z = 5$  with  $10^{10} \leq M_*/M_\odot \leq 10^{11.3}$  produced by SYNTHOBS. The top panel shows the intrinsic stellar SED in green and the dust attenuated SED (including LoS effects) in red. The lower panel shows the rest-frame top-hat photometric filters used throughout this analysis, plotted with an arbitrary y-axis to aid interpretation. The black lines correspond to the location and bandwidth of the *James Webb Space Telescope* (*JWST*)’s Near-Infrared Camera (NIRCam)’s reddest wide-band filter (F444W) at the indicated redshifts. This indicates the reddest rest-frame bands accessible by the *JWST* at high enough resolution to measure robust sizes with NIRCam (0.062 arcsec) at  $z > 5$ .

assumption from Charlot & Fall 2000 that birth clouds dissipate on these time-scales) to a H II region (or birth cloud). To include the LyC emission for each stellar particle we follow the approach detailed in Wilkins et al. (2020), in which the pure stellar spectrum is processed with the CLOUDY photoionization code (Ferland et al. 2017) assuming:

- (i) the H II region’s metallicity is identical to the stellar particle’s;
- (ii) dust depletion and relative abundances from Gutkin, Charlot & Bruzual (2016);
- (iii) a reference ionization parameter (defined at  $t = 1$  Myr and  $Z = 0.02$ ) of  $\log_{10}(U_{s, \text{ref}}) = -2$ ;
- (iv) a hydrogen density of  $\log_{10}(n_{\text{H}}/\text{cm}^{-3}) = 2.5$ ;
- (v) CLOUDY’s default Orion-type graphite and silicate grains.

### 3.1.3 Dust attenuation

To include the effects of dust attenuation from the interstellar medium (ISM) we adopt a line-of-sight (LoS) attenuation model. In this model we treat stellar particles as emitters along an LoS (in this paper, we select the  $z$ -axis of the simulation) and account for the attenuation due to gas particles that intersect this LoS. Using an LoS approach means stellar emission undergoes spatially resolved attenuation rather than the uniform attenuation of a simple screen model, enabling considerably more robust photometry.

To do this we find all gas particle SPH kernels that intersect the stellar particle’s LoS and integrate along it to get the metal column density,  $\Sigma(x, y)$ . We then link this metal column density to the ISM dust optical depth in the  $V$  band (550 nm),  $\tau_{\text{ISM}, V}(x, y)$ , with a similar

approach as in Wilkins et al. (2017). This gives the expression

$$\tau_{\text{ISM}, V}(x, y) = \text{DTM} \kappa_{\text{ISM}} \Sigma(x, y), \quad (3)$$

where DTM is the galaxy specific dust-to-metal ratio from the fitting function presented in Vijayan et al. (2019). This is a function of the mass-weighted stellar age ( $t$ ) and the gas-phase metallicity of a galaxy ( $Z$ ),

$$\text{DTM} = \mathcal{D}_0 + (\mathcal{D}_1 - \mathcal{D}_0) [1 - \exp(-\alpha Z^\beta (t/\tau)^\gamma)], \quad (4)$$

where  $\mathcal{D}_0$  and  $\mathcal{D}_1$  represent the initial Type II supernovae (SNe) dust injection and saturation, respectively, and  $\tau$  is an estimate of the initial dust growth time-scale after dust injection from Type II SNe but prior to the initiation of dust growth on grains.<sup>2</sup> The normalization factor  $\kappa_{\text{ISM}}$  was chosen to match the rest-frame ultraviolet luminosity function (UVLF) from Bouwens et al. (2015) and acts as a proxy for dust properties such as average grain size, shape, and composition ( $\kappa_{\text{ISM}} = 0.0795$ ). The FLARES simulations do not inherently model dust production and destruction, thus we have to resort to these data-driven proxies.

In addition to attenuation due to the ISM, young stellar populations ( $t < 10$  Myr) are still embedded in their birth clouds and thus need to take into account attenuation due to this cloud. For these young stellar particles we include the additional attenuation expression:

$$\tau_{\text{BC}, V}(x, y) = \kappa_{\text{BC}}(Z/0.01), \quad (5)$$

where  $Z$  is the metallicity of the young stellar particle and  $\kappa_{\text{BC}}$  is another normalization factor encapsulating the dust properties of the birth cloud, for this we assume a constant value of  $\kappa_{\text{BC}} = 1$ . For stellar particles older than 10 Myr,  $\tau_{\text{BC}, V}(x, y) = 0$  and there is no contribution. In Appendix D, we present sizes omitting this birth cloud contribution to quantify its effect on galaxy size.

We then combine these optical depths in the  $V$  band,

$$\tau_\lambda = (\tau_{\text{BC}, V} + \tau_{\text{ISM}, V}) \left( \frac{\lambda}{550 \text{ nm}} \right)^{-1}, \quad (6)$$

yielding an expression for the optical depth at other wavelengths that can be applied to the stellar particle SEDs to account for dust attenuation.

## 3.2 Image creation

We then apply top-hat photometric band filters to the SEDs producing photometry for each stellar particle. Using this photometry we produce synthetic observations with a field of view (FoV) of  $60 \times 60$  pkpc<sup>2</sup> encompassing the entire 30 pkpc aperture in which a galaxy’s integrated quantities are measured (corresponding to 9.34, 12.20, and 14.13 arcsec at  $z = 5, 8,$  and  $10$ , respectively); see Section 2.1. We adopt a resolution equal to the redshift-dependent softening length of the simulation ( $s = 2.66/(1 + z)$  pkpc). In Appendix C, we present a comparison of image resolutions.

Synthetic images are often created by treating each stellar particle as a two-dimensional Gaussian kernel. The standard deviation of this kernel can either be defined by the softening length ( $\sigma = s$ , producing minimal smoothing), the stellar particle’s smoothing length ( $\sigma = h_{\text{smi}}$ , accounting for the local density), or, most often, the proximity to the  $N$ th neighbouring stellar particle ( $\sigma = r_N$ ) (e.g. Torrey et al. 2015; Ma et al. 2018; Marshall et al. 2022). The full image is then

<sup>2</sup>For the parameters of this function we use the best-fitting values from Vijayan et al. (2019, see section 4.1.3 therein for further details):  $\mathcal{D}_0 = 0.008$ ,  $\mathcal{D}_1 = 0.329$ ,  $\alpha = 0.017$ ,  $\beta = -1.337$ ,  $\gamma = 2.122$ , and  $\tau = 5 \times 10^{-5}$  (Gyr)/( $\mathcal{D}_0 Z$ ).

a sum over these contributions. In this method an image ( $I$ ) can therefore be expressed mathematically as

$$I_i = \exp\left(-\frac{(X - x_i)^2 + (Y - y_i)^2}{2\sigma_i^2}\right), \quad (7)$$

$$I = \sum_{i=0}^{N_*} \frac{I_i L_i}{\sum_{\text{pix}} I_i}, \quad (8)$$

where  $I_i$  is the smoothed image (kernel) produced for the  $i$ th stellar particle,  $\sigma_i$  is the standard deviation of the  $i$ th stellar particle's kernel,  $X$  and  $Y$  are a grid of pixel positions,  $x_i$  and  $y_i$  are the  $i$ th stellar particle's  $x$ -axis and  $y$ -axis positions in the desired projection,  $L_i$  is the luminosity of the  $i$ th particle, and the sum in the denominator is a sum over all pixels for the  $i$ th stellar particle to normalize the kernel.

However, this approach not only differs from the SPH treatment of a stellar particle but is also extremely computationally expensive. Unless artificially truncated a Gaussian kernel encompasses the whole image, leading to insignificant but time-consuming calculations. In fact, in SPH simulations a stellar particle is treated as a representation of a fluid with the full extent of the stellar population described by a spline kernel with a definitive cut-off where the kernel falls to 0 (Borrow et al. 2022). Using a spline kernel-based approach is not only a better representation of the underlying simulation's treatment of stellar particles but also greatly reduces the size of the computation by limiting the number of pixels computed per stellar particle.

For these reasons we implement a method of smoothing employing the SPH kernel used in the simulation to describe a stellar particle's 'extent'. In the ANARCHY SPH scheme, used in the EAGLE model (Schaye et al. 2015), this kernel is the  $C_2$  Wendland kernel (Wendland 1995; Dehnen & Aly 2012). We therefore adopt this kernel in this work, but note that for other simulations the kernel corresponding to that particular simulation should be used to maximize the fidelity of this method.

As with the Gaussian approach, an image can be described as a sum over kernels; unlike the Gaussian approach however, the spline kernels are necessarily three-dimensional and need projecting into the  $x$ - $y$  plane. To achieve this we calculate the spline kernels on a voxel grid and sum over the  $z$ -axis,

$$I = \sum_{z\text{-axis}} \sum_{i=0}^{N_*} \frac{K_i}{\sum_{\text{vox}} K_i} L_i, \quad (9)$$

where each stellar particle's kernel ( $K_i$ ) is now

$$K_i = \frac{21}{2\pi} \frac{w_i}{h_{\text{sml}}^3}, \quad (10)$$

with the kernel  $w_i$  given by

$$w_i(q_i = r/h_i) = \begin{cases} (1 - q_i)^4 (1 + 4q_i), & q_i \leq 1, \\ 0, & q_i > 1, \end{cases} \quad (11)$$

where  $r$  is the distance between the particle and any given voxel within the kernel.

To compute this kernel efficiently we employ a KD-Tree algorithm, building a tree based on voxel coordinates. We query the tree for all non-zero pixels where the distance between the pixel and the stellar particle ( $r$ ) is less than the limits of the smoothing kernel (here  $r < h$ ), greatly reducing the computation from  $O(N_* N_{\text{pix}})$  in the Gaussian case to  $O(N_* N_{\text{vox}(r < h)})$  using the more representative spline approach.

In Fig. 2, we present a grid of randomly selected galaxy images in the far-UV filter along with their stellar mass (derived by summing the underlying particle distribution), luminosities, central surface densities, and half-light radii measured including the effects of dust.

It should be noted that throughout this analysis we do not rotate galaxies, instead adopting their existing orientation in the box to emulate the stochastic viewing angles of galaxies in the real Universe. Henceforth, all analysis derived from images will use this method of stellar particle smoothing (implemented from Section 4.2.2 onwards), unless explicitly stated otherwise. In Appendix A, we present comparisons between the Gaussian and spline approach for this simulation.

## 4 GALAXY SELECTION AND SIZE MEASUREMENT

In this section, we describe our galaxy sample, and describe the two measurement methods used to derive sizes.

### 4.1 Extracting the galaxy sample

To ensure all galaxies in the sample have enough particles to be considered morphologically resolved, we omit all subgroups with fewer than 100 stellar particles ( $N_* < 100$ ). We apply a 95 per cent completeness criterion, dividing the sample of galaxies into those above and below the completeness limits in mass and luminosity. These completeness limits are given by the mass and luminosity at which the galaxy sample is missing 5 per cent due to galaxies having  $N_* < 100$ . We adopt 95 per cent complete rather than 100 per cent complete to avoid the luminosity threshold being defined by anomalously bright galaxies with  $N_* < 100$ . These limits are presented in Table 1 at each redshift for the far-UV band. This ensures we present results motivated by a complete galaxy sample. We none the less present the incomplete sample at low opacity in all scatter plots for context.

We further distinguish between two morphological populations by applying a threshold derived from the intrinsic size–luminosity relation of  $S \geq 10^{29} \text{ erg s}^{-1} \text{ Hz}^{-1} \text{ pkpc}^{-2}$  to their central surface flux density (i.e. the surface flux density within the half-light radius). This threshold splits the sample into a population of centrally compact galaxies and a population of diffuse galaxies; in subsequent plots we will denote the compact population by coloured hexbins and the diffuse population by greyscale hexbins.

This division of the galaxy sample is shown in the mass–luminosity relation in Fig. 3 at  $z = 5$ ; here we have adopted the previously described colouring and have used opacity to distinguish the complete and incomplete populations. The dashed lines denote the completeness limits in mass and luminosity. The histograms on the axes show the galaxy distribution along each axis with the full galaxy population in grey and galaxies with  $N_* \geq 100$  shown in black.

All following plots will follow these plotting conventions, with greyscale colours denoting the diffuse galaxy distribution and coloured hexbins denoting the compact population (as defined by their central surface density). The hexbins themselves indicate the weighted number density of galaxies, using the weights derived in Lovell et al. (2021). All fits are performed on the complete sample. This division of the galaxy sample leads to:

- (i) 50 238 galaxies in the sample with more than 100 stellar particles (25 556, 2863, and 492 at  $z = 5, 8,$  and  $10,$  respectively);
- (ii) 7172 in the compact population with more than 100 stellar particles (2701, 696, and 240 at  $z = 5, 8,$  and  $10,$  respectively);
- (iii) 43 066 in the diffuse population with more than 100 stellar particles (22 855, 2167, and 252 at  $z = 5, 8,$  and  $10,$  respectively);
- (iv) 31 697 galaxies in total above the completeness limit (16 238, 1700, and 273 at  $z = 5, 8,$  and  $10,$  respectively).

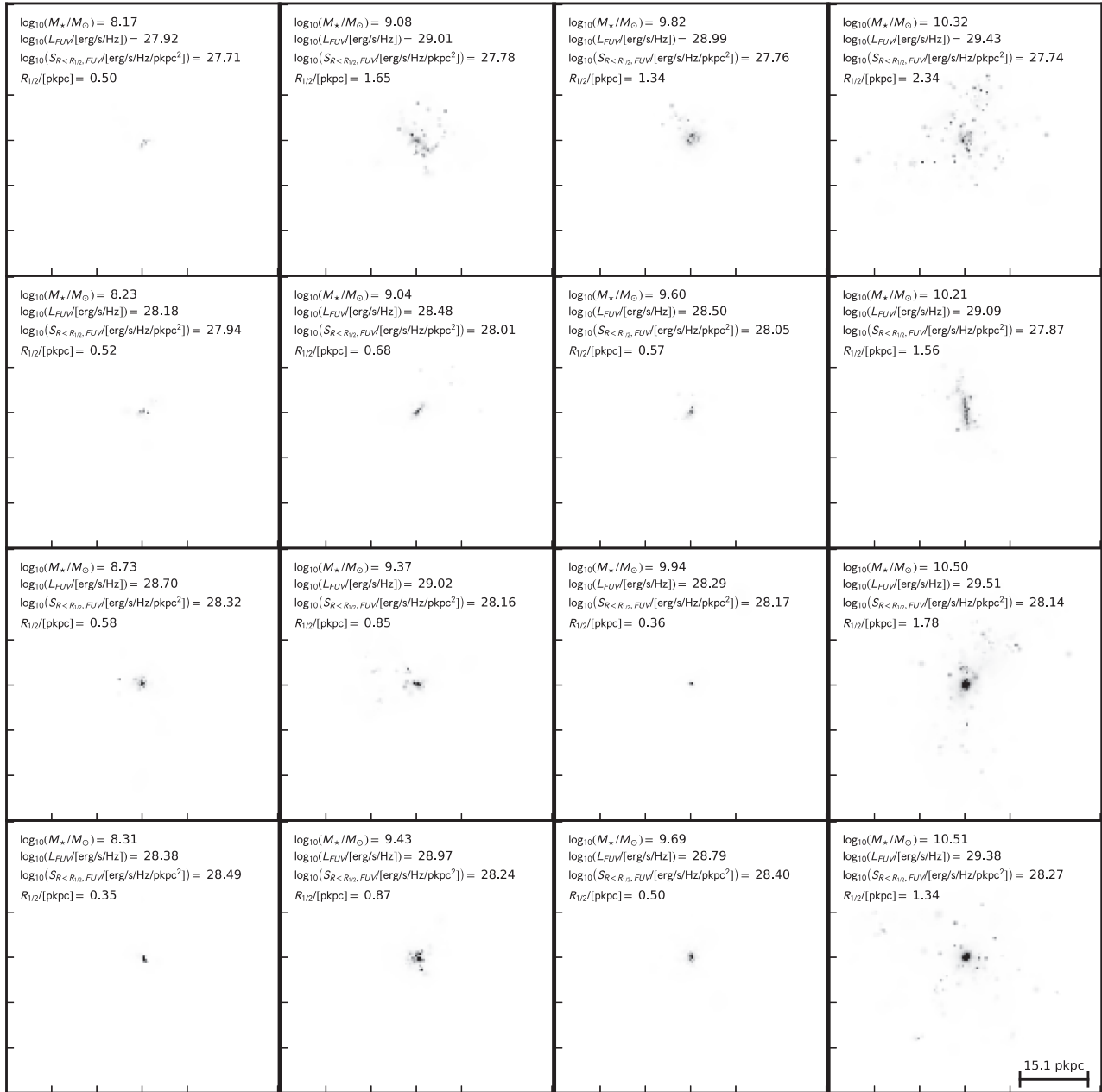


**Figure 2.** A subset of  $z = 5$  synthetic far-UV galaxy images computed using the method outlined in Section 3.2. Each panel is the full  $60 \times 60$  pkpc<sup>2</sup> FoV for each galaxy. Galaxies increase in mass left to right and increase in central surface density top to bottom. The pixel values of these images are linearly normalized across all panels with their mass, luminosity, central surface density, and half-light radius included in each panel. The galaxies included in this subset were randomly selected from each mass and central surface density bin, even so they display the variety of morphologies already present by  $z = 5$  in FLARES.

## 4.2 Size measurement methods

There are a myriad of methods used to define the sizes of galaxies present in the literature including Sérsic profile fitting (Sérsic 1963, 1968), curves of growth (e.g. Bouwens et al. 2004; Ferguson et al. 2004; Oesch et al. 2010), Petrosian radius (Petrosian 1976), and simulation specific methods that use the particle distribution to find the radius enclosing a percentage of the total mass/luminosity.

Each measurement method introduces its own dependencies and challenges. In this section, we detail and compare the two methods utilized in this analysis: a particle-based method, and a non-parametric pixel-based method (e.g. Ribeiro et al. 2016; Ma et al. 2018; Marshall et al. 2022). We neglect curves of growth, Petrosian

radius, and Sérsic profiles entirely; at these redshifts the clumpy nature of galaxies, particularly at lower masses (Jiang et al. 2013; Bowler et al. 2017), makes these methods unreliable. Throughout this work we use  $R$  to refer to the half-light radius (size) of a galaxy.

### 4.2.1 Particle-based method

We take the underlying particle distribution within a 30 pkpc aperture and find the radius of the particle bounding half the total luminosity inside this aperture. We then interpolate around this initial measurement to better sample the radial density profile, mitigating its discretization into individual, comparatively low resolution, particles.

**Table 1.** The mass and luminosity 95 per cent completeness limits for the galaxy sample in each redshift bin. The mass limits are consistent across all bands, but the luminosity limits are band specific. Here we present the far-UV (1500 Å) limits focused on for the majority of the analysis presented in this paper.

Redshift ( $z$ )	$\log_{10}(M/M_{\odot})$	$\log_{10}(L_{\text{int}}/[\text{erg s}^{-1} \text{ Hz}^{-1}])$	$\log_{10}(L_{\text{att}}/[\text{erg s}^{-1} \text{ Hz}^{-1}])$
12	8.16	28.60	28.43
11	8.15	28.55	28.42
10	8.15	28.52	28.39
9	8.14	28.46	28.34
8	8.13	28.40	28.28
7	8.13	28.31	28.19
6	8.12	28.24	28.12
5	8.11	28.16	28.03

It should be noted that this measurement method is sensitive to the chosen galactic centre; in this work we use the centre of potential calculated by SUBFIND. Other choices, such as the centroid, can give different results for diffuse and irregular structures since the centre of potential may be located within one of the clumps, which may not necessarily lie in the centre of the galaxy. This offset centre leads to larger size measurements, as the majority of the stellar material of the galaxy is offset from the centre from which the radius is measured.

In all plots including this measurement we take the luminosity to be the sum of each individual particle’s luminosity within the aperture, neglecting any smoothing over the SPH kernel.

#### 4.2.2 Pixel-based method

In the non-parametric pixel approach, the pixels of the image are ordered from most luminous to least luminous. We then find the pixel area containing half the total luminosity before converting to a radius assuming a circular area,  $R = \sqrt{A/\pi}$ , and then interpolating around this radius as in the particle method. Unlike the particle method this method of measurement has a minimum possible size where half the total luminosity falls within a single pixel, resulting in a radius of  $R_{\text{min}} = \sqrt{A_{\text{pix}}/\pi}$  before interpolation between 0 and  $R_{\text{min}}$ . The interpolation here allows for the measurement of half-light radii smaller than a single pixel, however this does not remove the limitation caused by the finite pixel resolution.

This method is particularly robust at high redshifts, where the independence from a centre definition and non-contiguous size definition better encapsulate the morphology of clumpy structures.

In all plots using this measurement we present the luminosities as detected from the image, i.e. the sum of all pixels within the FoV. This can subtly differ from the particle luminosities where a particle’s kernel extends beyond the bounds of the FoV, spreading the particles light outside the image in contrast to the particle-based method.

#### 4.2.3 Comparing particle and pixel methods

In Fig. 4, we present a comparison of these methods for the sizes of all galaxies at  $z = 5$  using their intrinsic luminosities. For the compact galaxies (colour) we see a reasonable correspondence between the two methods with a scatter around the 1:1 relation. However, as the size of a galaxy increases the particle method begins to produce larger sizes than the pixel method due to a combination of centring effects and luminous structures within the outskirts of galaxies, such as those shown in a number of panels in Fig. 2. Conversely, for the smallest galaxies, the pixel size is larger than the particle size; this is a manifestation of the stellar particle smoothing used in the creation

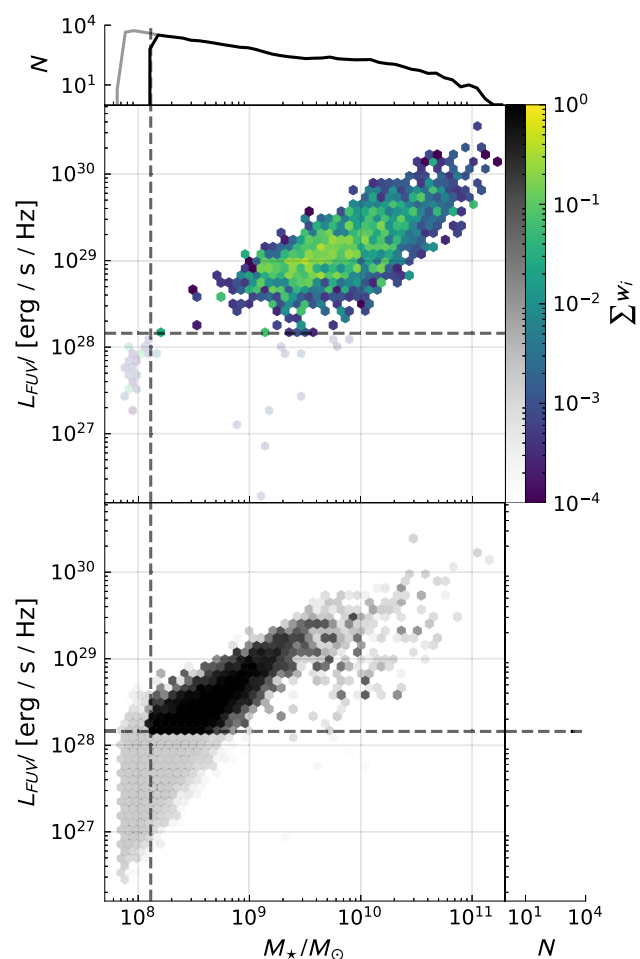


**Figure 3.** The intrinsic mass–luminosity relation at  $z = 5.0$ . The top panel of coloured hexbins is the galaxies in the compact population and the lower panel of greyscale points represents galaxies in the diffuse population, as described in Section 4.1. The dashed lines show the completeness limits for the galaxy sample with those galaxies that fall outside this completeness threshold denoted by low opacity. Each hexbin is coloured by the weighted number density of galaxies, using the FLARES region weighting scheme. The histograms on each axis show the total distribution of galaxies in both the compact and diffuse population along each axis, with the grey line showing all galaxies and the black line showing those with  $N_{\star} \geq 100$ .

of the images, where light concentrated in densely packed particles is smoothed over a larger pixel area.

For the diffuse (greyscale) population the scatter is more pronounced and extends towards larger particle values across the full range of sizes. This is because of the aforementioned strength of the pixel method when it comes to clumpy diffuse structures and the issue of defining a centre for these structures in the particle method. The size floor is also evident in the smallest galaxies in the diffuse (and incomplete) sample where a single pixel contains half the total luminosity of the dim galaxy.

## 5 SIZE–LUMINOSITY RELATIONS

Here we present results for the sizes of galaxies in the EoR. All plots that compare to observational quantities are derived from the pixel measurement method (Section 4.2.2) measured from the synthetic images detailed in Section 3.2. Intrinsic properties such as the intrinsic size–luminosity relation (Section 5.1) and half-dust

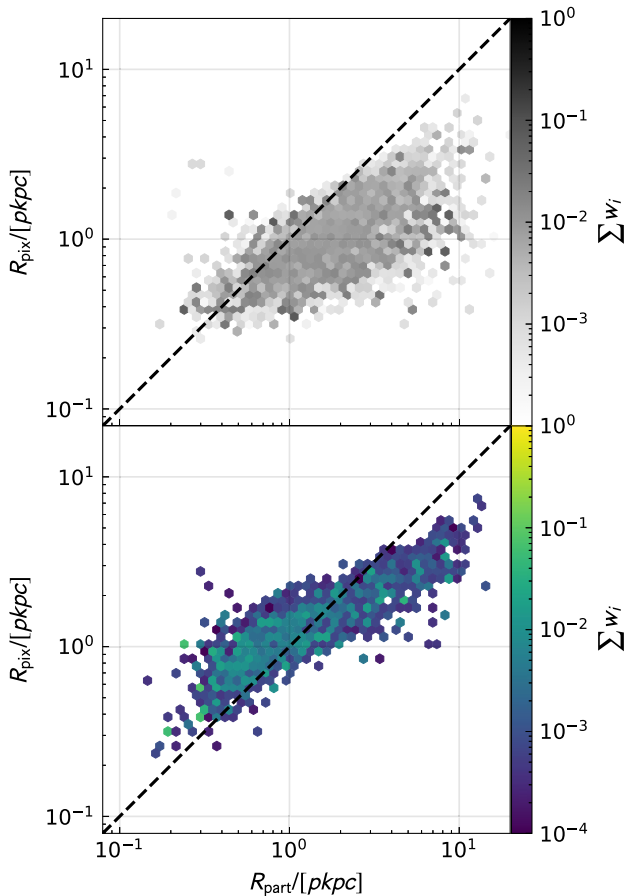


**Figure 4.** A comparison between the dust-attenuated half-light radii of galaxies at  $z = 5$  yielded by the particle measurement method ( $x$ -axis) and the pixel method ( $y$ -axis). The upper panel of greyscale points shows the diffuse galaxy population, while the lower panel of coloured points shows the compact galaxy population. The dashed black line corresponds to a 1:1 relationship. Each hexbin is coloured by the weighted number density of galaxies, using the FLARES region weighting scheme.

radius (Section 5.2.1) are measured using the particle method to focus on the intrinsic nature of these properties.

### 5.1 Intrinsic UV size–luminosity relation

Although impossible to probe in observations, we can use the intrinsic UV size–luminosity relation to trace the underlying stellar population in galaxies. Fig. 5 shows this relation at  $z = 5$  for the particle measurements. This shows two surprising features: two distinct populations, and a clear negative slope to the intrinsic size–luminosity relation.

Although the negative slope of the intrinsic size–luminosity relation is somewhat counter-intuitive, it has been seen at these redshifts in other recent simulations, particularly in BLUE TIDES (Marshall et al. 2022) with a negative size–mass relation at  $z = 7$  and ILLUTRIS-TNG (Popping et al. 2022) with a negative observed-frame  $850 \mu\text{m}$  size–mass relation at  $z = 5$ . Indeed, there are also hints in observations with evidence for a constant dependence between galaxy size and mass (Lang et al. 2014; Moseleh et al. 2020).

Here the division in central surface density is particularly evident. In terms of luminosity we have one dim ( $L \lesssim 10^{29} \text{ erg s}^{-1} \text{ Hz}^{-1}$ ) and more diffuse population, and one bright ( $L \gtrsim 10^{29} \text{ erg s}^{-1} \text{ Hz}^{-1}$ ) and compact ( $R_{1/2} \lesssim 1 \text{ pkpc}$ ) population.

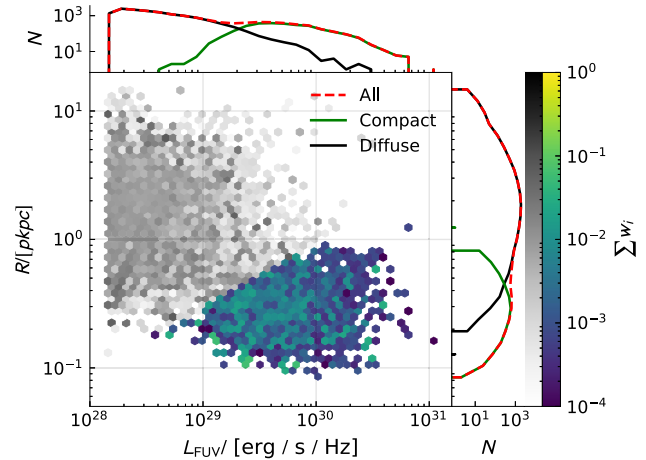


**Figure 5.** The intrinsic UV size–luminosity relation at  $z = 5$ , measured using the particle method. Showing the dimmer diffuse population in greyscale and the bright compact population in colour. The hexbins are coloured by the sum of FLARES region weightings for each individual galaxy, making each hexbin a weighted number density in the UV size–luminosity plane. Histograms showing the one-dimensional distributions of the two populations and the complete sample are plotted along each axis with the compact population in solid green, the diffuse population in solid black, and the complete sample in dashed red.

As shown in Furlong et al. (2017), the EAGLE low-redshift intrinsic size–mass relation, a good tracer for the intrinsic size–luminosity relation, is positively sloped with a good agreement with observational results. Below we briefly outline the physical mechanisms in FLARES and the EAGLE model that cause the bimodality and negative intrinsic size–luminosity relation at high redshift, and how they evolve leading to the results in the low-redshift regime. We will present our investigation into the physical mechanisms governing the cause and evolution of the two populations in detail in an upcoming paper.

(i) At  $z \gtrsim 5$ , galaxies that reach  $M/M_{\odot} \gtrsim 10^9$  develop extremely dense cores and begin a spike in core star formation at high stellar birth densities.

(ii) This begins to seed the gas in the galaxy’s core with metals, increasing the effectiveness of metal line cooling, inhibiting stellar and AGN feedback, and further driving star formation.

(iii) This overcooling causes a feedback loop of star formation in the galaxy’s core, allowing the galaxy to become massive and ultracompact during this early epoch.

(iv) While this process takes place in the galaxy’s core the galaxy accretes an extended gas distribution up to 100 times larger than the stellar distribution. Because of the high densities in the core, stellar feedback is unable to mix the core’s metals into this surrounding gas distribution. This lack of metals inhibits cooling and leaves the extended gas distribution unable to efficiently form stars.

(v) At  $z \lesssim 4$  the extended gas distribution reaches the density and metallicity necessary for efficient star formation. This is facilitated partly by their own collapse and partly due to the growing efficiency of stellar and AGN feedback (Crain et al. 2015), mixing metals from the core into the surroundings. This extended star formation manifests as an increase in intrinsic galaxy size at late times, yielding a positively sloped intrinsic size–luminosity relation.

In the upper panel of Fig. 6, we present a stack of the central intrinsic emission of all galaxies at  $z = 5$  in FLARES (irrespective of completeness) split into mass bins of  $\log_{10}(M/M_{\odot}) = [8-9, 9-9.5,$

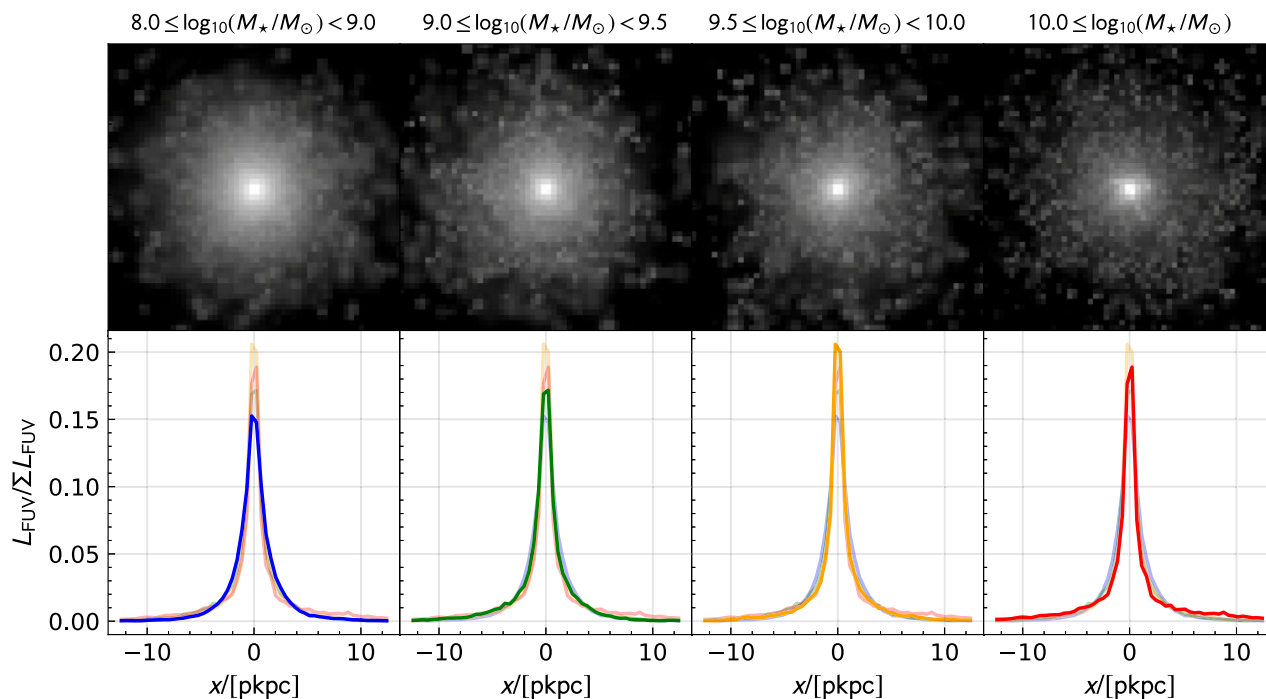


**Figure 6.** The upper panel contains stacked individually log-scaled images of the intrinsic luminosity of every galaxy in our complete galaxy sample at  $z = 5$ . These stacks cover the central  $\sim 24$  pkpc of the image and are split into mass bins (increasing left to right). The lower panels show one-dimensional profiles of these stacks. The luminosity on the y-axis of these profiles is normalized to the sum of each stacked image. In each panel all profiles are plotted with the curves corresponding to the other panels plotted in low opacity to aid interpretation.

9.5–10,  $>10$ ]. This qualitatively shows how the negative gradient in the size–luminosity relation translates to the compactification of a galaxy’s intrinsic emission in relation to a galaxy’s mass. In the lower panel of Fig. 6, we plot one-dimensional profiles of the stacked mass bin images to explicitly show the compactification. As with the stacked images, the profiles exhibit a narrowing and increasing central concentration with increasing mass. The overcooling begins to take effect between the leftmost mass bin ( $10^8 < M/M_\odot < 10^9$ ) and the next mass bin of  $10^9 < M/M_\odot < 10^{9.5}$ . At this crossover between regimes there is a narrowing of the profile and stronger concentrated peak, which becomes more peaked as the mass increases. The growth of this central peak then drops off in the final mass bin due to an increased contribution by the wings of the profile; galaxies in this mass bin exist in the most dense environments and thus include more luminous substructure at large radii.

In Fig. 7, we show the mass dependence of the half-light radii shown in Fig. 5 and exponential fits to profiles derived from intrinsic stacked images, such as those shown in Fig. 6, split into mass bins of  $\Delta M = 10^{0.4} M_\odot$ . Stacking the images mitigates the issue raised by clumpy structures at high redshift, as detailed in Section 4.2, enabling exponential profile fitting. The scale lengths follow the same negative trend as the intrinsic half-light radii with smaller sizes at low masses relative to the half-light radii. The exponential profiles fit the central regions of the stacks well but fail to fit the profile in the wings, hence the smaller scale lengths for the most diffuse galaxies.

## 5.2 The effects of dust

We now move on from the intrinsic size–luminosity relation to discuss the effects of dust on the observed UV size–luminosity relation. All plots from this point on will present the pixel measured sizes unless explicitly stated otherwise.

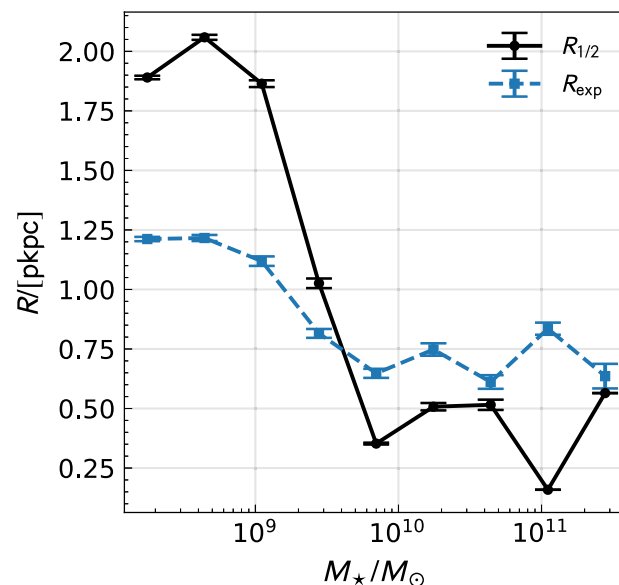


**Figure 7.** A comparison of the mass dependence of intrinsic half-light radii and exponential profile scale length. Similarly to the profiles in Fig. 6, the exponential profiles are fit to stacked images of the intrinsic emission in mass bins of  $\Delta M = 10^{0.4} M_\odot$  and are denoted by blue squares. The intrinsic half-light radii are derived from the distribution in Fig. 5 and denoted by black points. The error bars are derived from the fit and the standard error in each mass bin for the exponential profiles and the half-light radii, respectively.

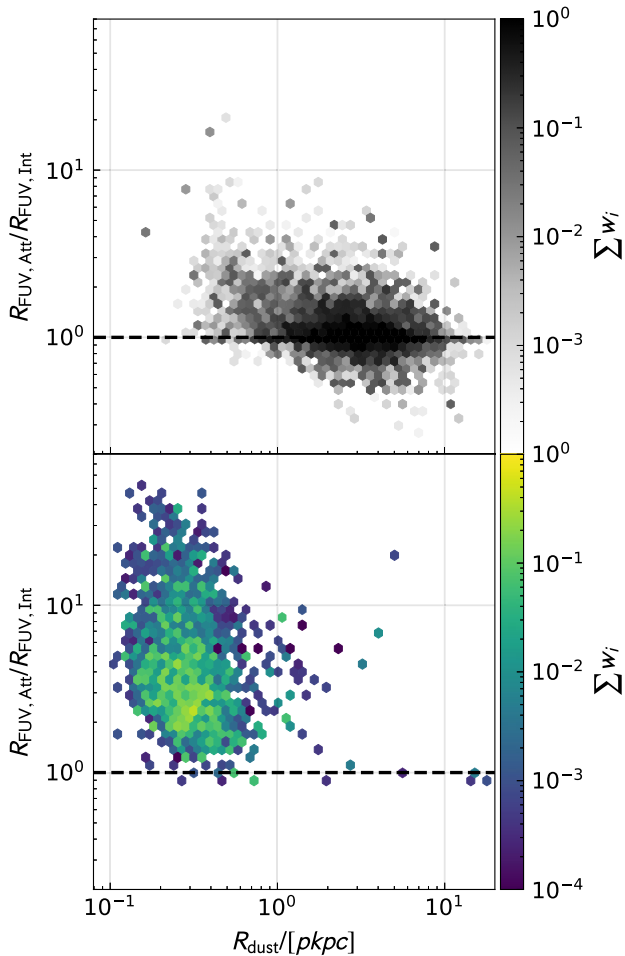


**Figure 8.** The ratio between dust attenuated and intrinsic size as a function of the half-dust radius (the radius enclosing half the mass in gas-phase dust) for all galaxies at  $z = 5$ , computed using the particle method. Once again, the galaxy sample is divided into the diffuse population (upper, greyscale) and the compact population (lower, coloured) and the hexbins are coloured by the cumulative weighting of each galaxy within a hexbin.

### 5.2.1 The distribution of dust

Dust attenuates the intrinsic stellar emission making observations of the pure stellar emission impossible. The affect this obfuscation will have on the measured size of a galaxy is sensitive to the spatial distribution of dust in a galaxy: a uniform screen would have no discernible effect on the size, whereas any concentration of dust in a particular region will have important consequences for the spatial distribution of observed stellar emission, and therefore perceived size.

We probe the underlying dust distribution in these galaxies by calculating the half-dust radius (i.e. the radius enclosing half the mass in gas-phase dust). To calculate the gas-phase dust mass we use the metallicity of each gas particle and multiply by the galaxy specific DTM (described in Section 3.1.3) to get the dust mass of each gas particle.

Fig. 8 shows the ratio between attenuated and intrinsic particle-based sizes as a function of this half-dust radius at  $z = 5$ . Galaxies in the compact population (coloured hexbins) have dust distributions with  $R_{1/2, \text{dust}} \lesssim 1$  pkpc and  $R_{\text{att}}/R_{\text{int}} \gtrsim 1$ . This indicates that, in the compact galaxy sample, not only is the distribution of dust highly concentrated in the core of the galaxy, but also the more

concentrated the dust, the larger the increase in observed size due to the attenuation of the galaxy’s bright core.<sup>3</sup> With the central regions strongly attenuated, the more extended regions are able to contribute more to the total luminosity of the galaxy, increasing the perceived size. In the most extreme cases, galaxies can appear  $\sim 50$  times larger when including dust attenuation. There are hints of this behaviour in observations at high redshift ( $z \sim 7$ ) with Bowler et al. (2022) demonstrating that between 35 and 75 per cent of a galaxy’s SFR is obscured by dust and is often highly compact, pinpointing the most star-forming regions in a galaxy.

The vast majority of the diffuse galaxy population (greyscale) also have diffuse dust distributions ( $R_{1/2, \text{dust}} > 1$  pkpc) and exhibit a more conservative increase in size between intrinsic and attenuated size. Compared to the compact population, the more diffuse dust distributions (and galaxies) have a flatter relation between the ratio of sizes and half-dust radius. Both the smaller increase in size and the flattening of this relation can be explained by a more uniform distribution of dust in these diffuse clumpy structures.<sup>4</sup>

Galaxies that fall below the dashed line, indicating a ratio of 1, represent a decrease in size with the inclusion of dust effects. These are instances where the dust is more uniformly distributed, and results in greater attenuation of their extremities, driving down the apparent size.

### 5.2.2 The observed UV size–luminosity distribution

The negative gradient in the intrinsic size–luminosity relation presented in Fig. 5 is in direct conflict with observational results that necessarily include the effects of dust attenuation (e.g. Hathi et al. 2008; Grazian et al. 2011, 2012; Kawamata et al. 2015, 2018; Shibuya et al. 2015; Calvi et al. 2016; Morishita et al. 2018; Bridge et al. 2019; Bouwens et al. 2022; Yang et al. 2022). However, in Section 5.2.1, we have shown that the inclusion of dust attenuation can result in large increases in size for the most intrinsically compact galaxies. Ascertaining if this effect is enough to yield sizes in line with observations is imperative to probe the validity of the negative intrinsic size–luminosity relation, and thus the physical models used in FLARES.

To compare to the observed results we use the method detailed in Section 3.2 for synthetic image creation and the pixel measurement method (Section 4.2.2) to produce the observed size–luminosity relation and compare to a wide array of observations in integer redshift bins from  $z = 5$  to 9. This observed size–luminosity relation is shown in Fig. 9.

Evidently, the concentration of dust in compact cores and increase in size between intrinsic and attenuated sizes, detailed in Section 5.2.1, has completely reversed the slope of the size–luminosity relation relative to the intrinsic relation.

Focusing on the high central surface density distribution (coloured hexbins), beyond the positive relation between size and luminosity, we can already see a power-law relation with minimal scatter. This

<sup>3</sup>This strong attenuation of the core justifies the omission of the AGN contribution to the UV luminosity. We have confirmed the AGN contribution is heavily attenuated at these wavelengths, in fact only a handful of galaxies in the sample have AGN that are comparable to their host galaxy in the UV luminosity.

<sup>4</sup>Those galaxies in the diffuse population that do not follow this trend (i.e. exhibit large increases in size with the inclusion of dust and have compact dust distributions) are galaxies very close to the central surface flux density threshold used to split the populations.

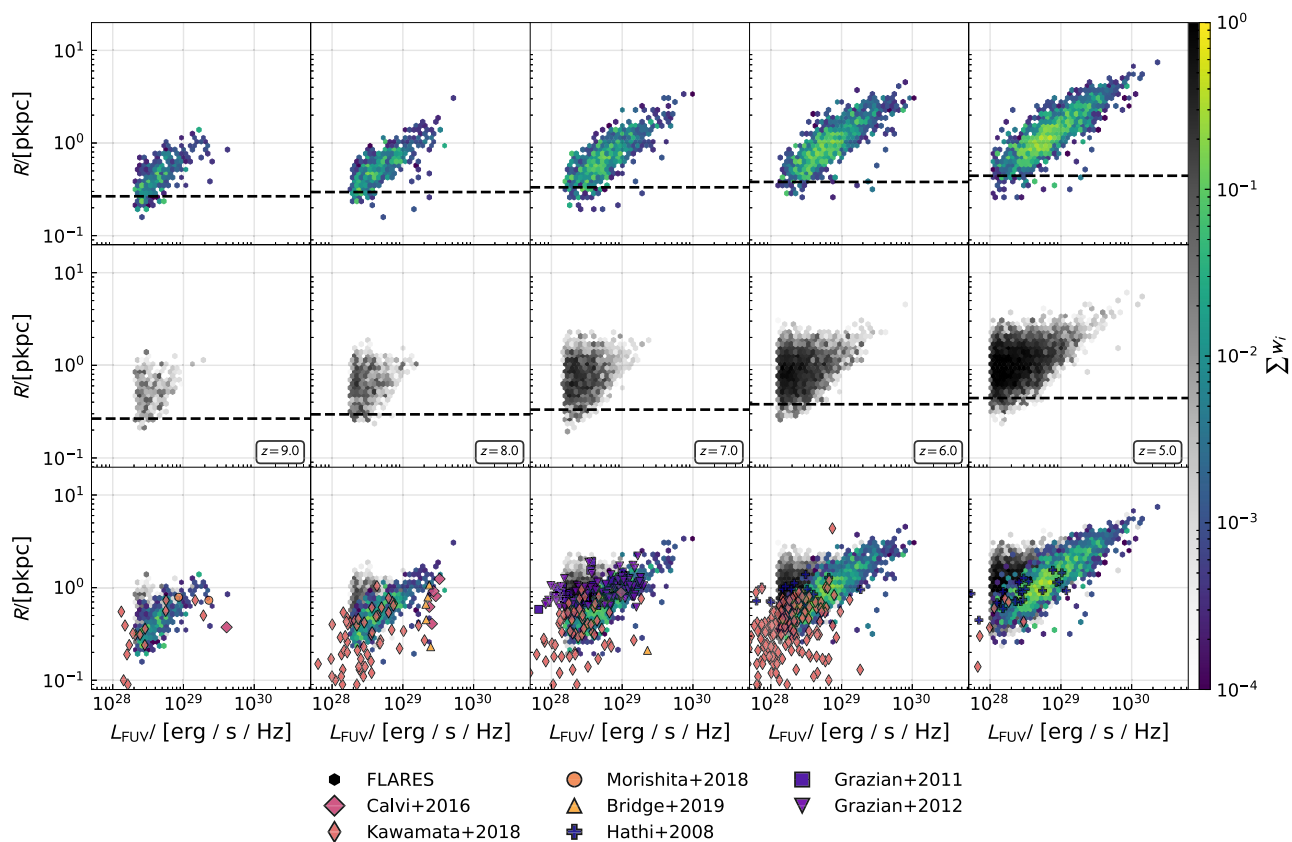


**Figure 9.** The attenuated far-UV (1500 Å) size–luminosity relation measured using the pixel method. The hexbins are again coloured by the weighted number density. The galaxy sample is divided into the compact galaxy population (top row, colour) and the diffuse galaxy population (middle row, greyscale). The dashed line shows the pixel resolution of the images used to make the FLARES measurements. Galaxies can fall below this line due to the interpolation used in the calculation of the pixel half-light radius. The bottom row contains both galaxy populations with a comparison to high-redshifts observations using the *Hubble Space Telescope* (Hathi et al. 2008; Grazian et al. 2011, 2012; Calvi et al. 2016; Kawamata et al. 2018; Morishita et al. 2018; Bridge et al. 2019).

scatter is increased for the diffuse, low central surface density population (greyscale hexbins), particularly for low-luminosity galaxies that exhibit a large range of sizes at fixed luminosity. We can also see that the FLARES galaxy sample extends to larger sizes and higher luminosities than the observed results, this is because of FLARES’s focus on rare and extreme environments where the most luminous galaxies reside.

There is a fair agreement between the scatter of observational measurements and the FLARES distribution with the exception of galaxies in the Kawamata et al. (2018) (lensed) sample that have sizes smaller than the resolution of FLARES. Particularly evident when comparing the FLARES and observational scatter are the Grazian et al. (2011) and Hathi et al. (2008) (dropout selected) points at  $z = 7$  and 6, respectively, with similar normalization to the low central surface density galaxies that scatter further from the power-law relation evident in the compact population. This could be tantalizing observational evidence for the galaxies that populate the diffuse population.

To quantify the agreement between the observational scatter and the FLARES sample we use CURVE\_FIT (non-linear least-squares fitting), from SCIPY (Virtanen et al. 2020), to produce fits of the form of equation (1). The results of this fitting are shown in Table 2.

Fig. 10 shows a comparison of these fits (solid red lines) to fits from observed samples: Huang et al. (2013) at  $z = 5$ ; Holwerda et al. (2015) at  $z = 7$  and 9; Kawamata et al. (2018) at  $z = 6$ –9; Bouwens et al. (2022) at  $z = 6$ –8; and Yang et al. (2022) at  $z = 6$ –7, the latter three of these including lensed sources. We also compare

**Table 2.** The fitting results for equation (1) for each redshift bin in Fig. 10 for the attenuated size–luminosity relations, measured using the pixel method (Section 4.2.2).  $R_0$  is a normalization factor, and  $\beta$  is the slope of the size–luminosity relation.

Redshift ( $z$ )	$R_0$ /(pkpc)	$\beta$
9	$0.793 \pm 0.019$	$0.519 \pm 0.026$
8	$0.842 \pm 0.012$	$0.319 \pm 0.013$
7	$1.126 \pm 0.011$	$0.290 \pm 0.008$
6	$1.370 \pm 0.007$	$0.279 \pm 0.004$
5	$1.692 \pm 0.006$	$0.300 \pm 0.003$

to two simulations: the MERAXES semi-analytic model (SAM; Liu et al. 2016; Marshall et al. 2019) at  $z = 5$ –9; and the BLUETIDES simulation (Marshall et al. 2022) at  $z = 7$ –9. We denote observations by dashed lines and simulations (other than FLARES) by dotted lines. Each fit is plotted using their published fitting parameters.

At  $z > 7$  the FLARES fits exhibit a good agreement in slope with the observational studies including lensed samples. These fits are significantly steeper than the observational samples that do not have a contribution of lensed galaxies, as demonstrated in Bouwens et al. (2022). At  $z \leq 7$  the FLARES fits begin to flatten relative to the studies including lensed sources as galaxies in the dim and diffuse size–luminosity regime become more numerous.

Compared to BLUETIDES, we find FLARES has a steeper size–luminosity relation at  $z = 8$ –9 and a stronger redshift evolution in

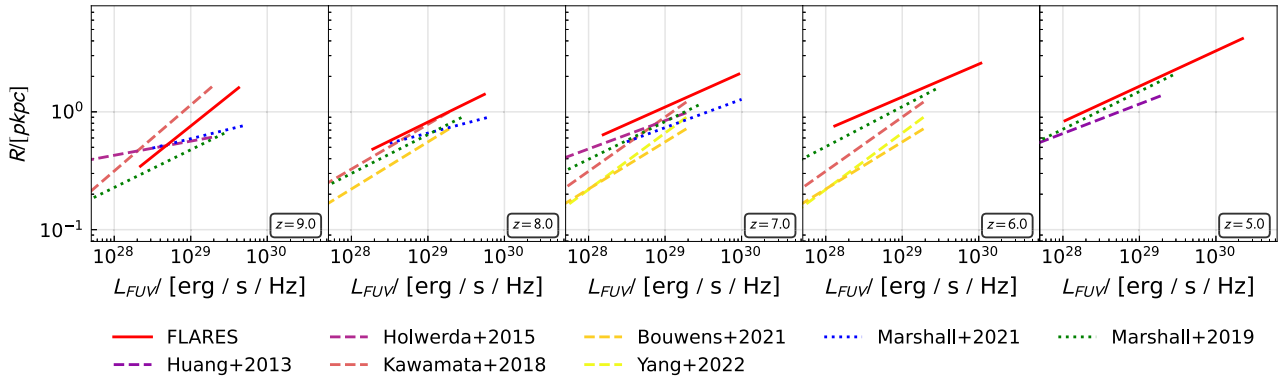


**Figure 10.** Fits to the UV size–luminosity relation including the effects of dust measured using the pixel method. To perform the fits we use the entire complete galaxy sample. We include comparisons to observations without lensed galaxies (Huang et al. 2013; Holwerda et al. 2015), observations including lensed sources (Kawamata et al. 2018; Bouwens et al. 2022; Yang et al. 2022), and simulations (Marshall et al. 2019, 2022). We denote FLARES by a red solid line, observations by dashed lines, and other simulations by dotted lines.

the normalization over the redshift range  $7 \leq z \leq 9$ . With respect to MERAXES we find a good agreement in slopes at  $z < 9$  with a consistently higher normalization at all redshifts.

Each work predicts a different normalization of the size–luminosity relation. This is particularly evident at  $z < 8$  where FLARES has consistently higher normalization than all other studies. One explanation for this difference is the resolution and measurement methods in each study. The pixel method used in this work is sensitive to the resolution of the image (for which we adopt the softening length of the simulation), observational studies on the other hand use images with a higher resolution than the softening length of FLARES and use an array of measurement techniques that are less sensitive to the pixel resolution. BLUETIDES uses the pixel method but adopts a higher pixel resolution below the softening length of the simulation, and MERAXES derive their sizes (scale radius of the disc) from the SAM galaxy properties. In addition to methodological differences, there is likely a significant contribution to the normalization by the diffuse galaxies, which at fixed luminosity extend to larger sizes in the FLARES sample.

The slopes reported in Table 2 for the attenuated size–luminosity relation are in broad agreement with the results of Grazian et al. (2012), Huang et al. (2013), Holwerda et al. (2015), Shibuya et al. (2015), Kawamata et al. (2018), Bouwens et al. (2022), and Yang et al. (2022) in various different redshift regimes. At  $z > 7$  the FLARES results exhibit the steeper slopes present in Kawamata et al. (2018), Bouwens et al. (2022), and Yang et al. (2022) before flattening into closer agreement with Grazian et al. (2012), Huang et al. (2013), Holwerda et al. (2015), and Shibuya et al. (2015) at  $z \leq 7$ . Again, this is due to the aforementioned compact low-luminosity galaxies present in the lensed samples, which are absent from the other studies, and the diffuse low-luminosity galaxies in the FLARES sample that become more numerous with decreasing redshift.

Many of the compact galaxies that strongly affect the slope of the size–luminosity relation in lensing studies fall below the resolution limit of FLARES (indicated by the dashed line in Fig. 9) and BLUETIDES. Higher resolution simulations are necessary to ascertain if these galaxies are present in the simulated sample and produce the same steepening behaviour. All observational samples also lack the most diffuse galaxies in the simulated samples due to their low surface densities. These would act to flatten the size–luminosity relation if present. Future works will aim to address both these issues with higher resolution simulations and fully synthetic observations including survey limits, instrument noise, point spread functions, and

observational methods of structure detection; the former addressing the missing dim and compact galaxies in the simulated sample and the latter addressing the diffuse galaxies that are likely undetected in the observational sample.

### 5.3 The size–luminosity relation as a function of wavelength

In Fig. 11, we present the size–luminosity relation across a range of rest-frame filters (shown in Fig. 1), and compare to the corresponding fits from Marshall et al. (2022) at  $z = [8, 7]$ . We present the fitting parameters in Appendix B.

As the probed wavelength regime reddens, the slope of the size–luminosity relation decreases, becoming increasingly negative for the reddest filters. These red filters probe the underlying stellar distribution with the least attenuation. The increasing representation of the underlying intrinsic distribution is clearly shown in the bottom row of panels as the slope of the ratio between attenuated and intrinsic size flattens with increasing wavelength. The slope of the size–luminosity relation for the reddest filters increases with decreasing redshift, implying that the intrinsic stellar population is becoming more diffuse as galaxies evolve.

This variation with wavelength is also predicted by BLUETIDES (Marshall et al. 2022) at  $z = [7, 8]$ , although they predict a shallower size–luminosity relation for the reddest filters relative to those produced in this work. It is also consistent with observations at low redshift (e.g. La Barbera et al. 2010; Kelvin et al. 2012; Vulcani et al. 2014; Kennedy et al. 2015; Tacchella et al. 2015).

None the less, these results present a tantalizing prediction that will allow the *JWST* to ascertain the validity of the negative intrinsic size–luminosity relation. The *JWST*’s reddest broad-band Near-Infrared Camera (NIRCam) filter (F444W) will probe as blue as the *B* band at  $z = 9$  and *I* band at  $z = 5$  (as shown in Fig. 1) allowing for high-resolution measurements of galaxy sizes in this regime.

### 5.4 Redshift evolution

In the literature there has been a wide range of presented methods for measuring the redshift evolution of galaxy sizes, with various approaches and galaxy sample definitions used for the computation. To produce a comprehensive comparison with FLARES we employ non-linear least-squares fitting (again using `SCIPY.CURVE_FIT`) to produce fits to equation (2) from various sample definitions pulled from the complete galaxy sample, all weighted with the FLARES

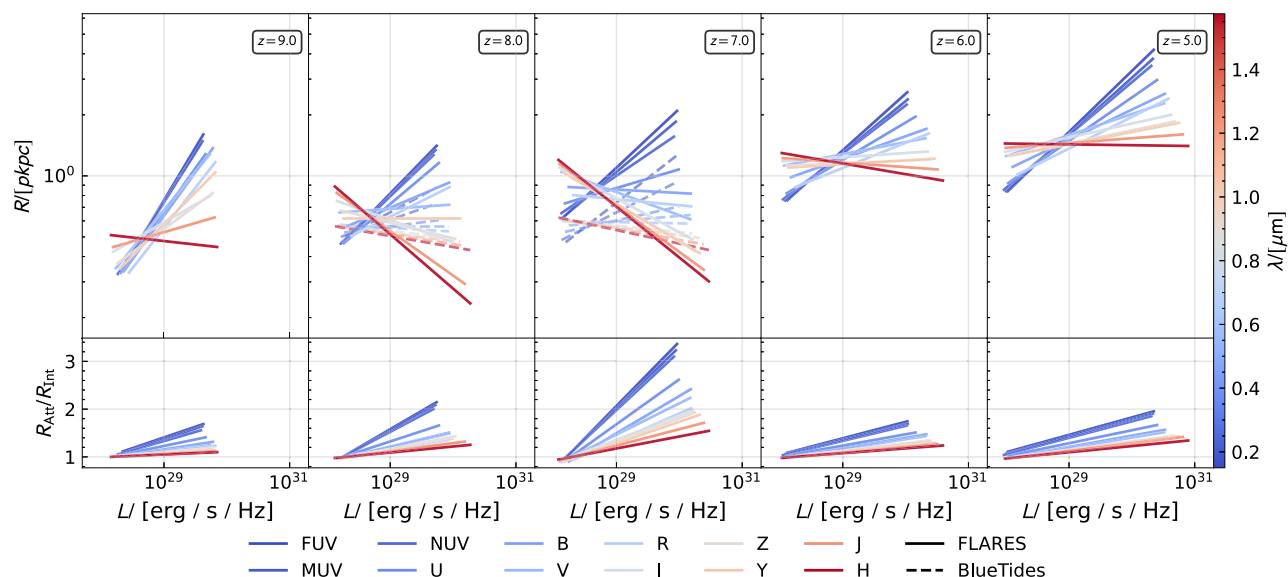


**Figure 11.** The upper row of panels shows fits to the size–luminosity relation for all rest-frame bands in Fig. 1. Solid lines represent the FLARES fits while dashed lines show the BLUE TIDES (Marshall et al. 2022) fits for the same selection of bands. The lower row of panels shows straight line fits to the ratio between the intrinsic and attenuated sizes for each band. The colour of the line denotes the band, with the bluest bands in blue and reddest bands in red. The colour bar shows the central wavelength of each rest-frame band in microns.

**Table 3.** The fitting parameters for equation (2) in Fig. 12 split into three redshift samples. From left to right: the full FLARES sample, a sample excluding the highest redshifts where robust observations are sparse, and a sample excluding the lowest redshift snapshots for comparison to BLUE TIDES.  $R_{0,z=0}$  is a normalization factor corresponding to a galaxy’s size at  $z = 0$ , and  $m$  is the slope of the redshift evolution.

Sample	$5 \leq z \leq 12$		$5 \leq z \leq 10$		$7 \leq z \leq 12$	
	$R_{0,z=0}/(\text{pkpc})$	$m$	$R_{0,z=0}/(\text{pkpc})$	$m$	$R_{0,z=0}/(\text{pkpc})$	$m$
$L < 0.3L_{z=3}^*$	$8.99 \pm 0.42$	$1.20 \pm 0.03$	$8.65 \pm 0.41$	$1.18 \pm 0.03$	$311.78 \pm 73.80$	$2.88 \pm 0.11$
$0.3L_{z=3}^* < L < L_{z=3}^*$	$21.98 \pm 1.04$	$1.59 \pm 0.03$	$21.53 \pm 1.04$	$1.58 \pm 0.03$	$49.91 \pm 7.62$	$1.99 \pm 0.07$
$0.3L_{z=3}^* < L$	$34.61 \pm 2.08$	$1.78 \pm 0.03$	$34.11 \pm 2.09$	$1.77 \pm 0.03$	$66.22 \pm 12.43$	$2.09 \pm 0.09$

weighting scheme. The results of this fitting are presented in Table 3.

In Fig. 12, we present these fits for a number of different sample definitions found in the literature. Fig. 13 shows a comparison of the slope ( $m$ ) from various studies, left to right: FLARES, Marshall et al. (2022), Oesch et al. (2010), Holwerda et al. (2015), Kawamata et al. (2018), and Ono et al. (2013), with a shaded region representing the range of slopes from Ma et al. (2018). We present the fitting parameters for these fits in Table 3.

For the low-luminosity sample we see a good agreement in slope between FLARES and Oesch et al. (2010) and Ono et al. (2013). For the other FLARES samples we find comparatively high slopes compared to the other works. However, these values are in agreement with Ma et al. (2018) who predict values in the range  $m = 1\text{--}2$  depending on the fixed mass or luminosity regime (shown by the shaded region). All but the low-luminosity sample’s slopes are larger than the evolution of systems at fixed circular velocity, implying an increasing feedback contribution to the evolution with decreasing redshift. Conversely, the low-luminosity sample’s evolution is closer to that of a system at fixed mass with the same additional feedback contribution. As feedback becomes more efficient with decreasing redshift the star-forming gas will be given more thermal energy and thus change the dynamics of the star-forming gas, increasing the radii at which stars can form and thus the half-light radii.

Limiting the included redshifts in the FLARES sample cannot only be used to compare to the more limited samples of BLUE TIDES, with

no galaxies at  $z < 7$ , and observations, where  $z \geq 10$  galaxies are exceedingly rare, but can also probe the evolution of size during particular epochs. To do this we limited the sample to a high- $z$  sample limited to  $z \geq 7$  and a low- $z$  sample with  $z \leq 10$ , the results of which are also included in Table 3. Limiting to  $z \geq 7$  resulted in a large increase in the slope of the redshift evolution alongside unrealistically high normalizations, predicting  $z = 0$  sizes of the order  $\sim 300$  pkpc for the low-luminosity sample and over double the  $z = 0$  size in the limited and high-luminosity samples in the other redshift selections. Conversely, limiting to  $z \leq 10$  instead results in fitting results consistent with those produced by the full redshift range. This casts doubt on the sparse  $z > 10$  measurements in observations causing the differences in slope between the FLARES measurement and observational measurements. More interestingly the differences in fits between redshift regimes imply a significantly faster evolution of galaxy size at the earliest times, even for the most dim and diffuse galaxies in the low-luminosity sample. It is clear from Fig. 12 that a piecewise fit produces a considerably better fit to the data than fitting across the entire redshift range.

Tensions between FLARES and the observations are far less stark than those between FLARES and BLUE TIDES samples but are none the less evident for the capped and high-luminosity samples, we do however see a good agreement in the low-luminosity sample. The tensions here could be explained by how sparse observations are at the highest redshifts due to the small area covered at the required depth; given that the low-luminosity sample in FLARES is also sparse

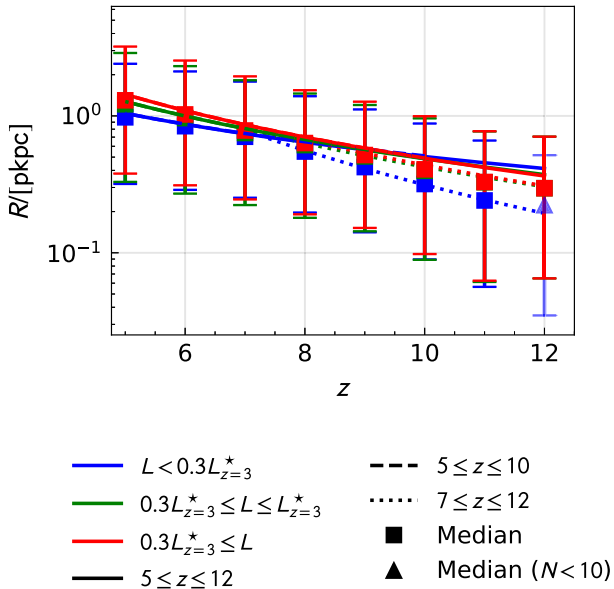


**Figure 12.** The redshift evolution of galaxy size in the FLARES sample split into three luminosity samples used in the literature: a low-luminosity sample,  $L < 0.3 L_{z=3}^*$  (blue), an intermediate-luminosity sample,  $0.3 L_{z=3}^* < L < L_{z=3}^*$  (green), and a bright galaxy sample,  $0.3 L_{z=3}^* < L$  (red), where  $L_{z=3}^* \approx 10^{29} \text{ erg s}^{-1} \text{ Hz}^{-1}$ . We present three different fits to the different redshift regimes: a solid line fit to the entire redshift range ( $5 \leq z \leq 12$ ), a dashed line fit to a low-redshift sample ( $5 \leq z \leq 10$ ), and a dotted line fit to a high-redshift sample ( $7 \leq z \leq 12$ ). The low- $z$  fits and the full redshift range fits almost entirely overlap. The points show the median in each redshift bin with error bars denoting the 16th and 84th percentile, a square point denotes more than 10 galaxies in the bin, and a triangle denotes less than 10 galaxies present in the sample at that redshift.

at the highest redshifts, the agreement between observations and FLARES here could be due to this luminosity regime being where the simulation and observations have the largest overlap in sampling strength. Additional observations from upcoming observatories populating the highest redshifts will increase the area and depth sampled in at this epoch and could rectify this tension. It should also be noted however that subgrid models require intensive investigation at this epoch, with comparison to robust observations to ascertain the validity of their behaviour. Future work will be able to converge the results of both simulations and observations to a consistent story of galaxy size evolution.

## 6 CONCLUSIONS

In this paper, we have presented an analysis of galaxy sizes at  $z \geq 5$  in the FLARES simulations across a wide array of environments. To do this we produced synthetic galaxy images using photometry in rest-frame UV and visual bands derived using the LoS attenuation method presented in Vijayan et al. (2021). We presented an efficient method of image computation by utilizing a KD-Tree of pixel coordinates and smoothing stellar particles over their SPH kernels. We employed this imaging method to produce synthetic galaxy images, from which the size of galaxies were measured using a non-parametric pixel-based method to account for the clumpy nature of galaxies at high redshift.

Using these measurements we probed both the intrinsic and observed size–luminosity relation in the rest-frame far-UV (1500 Å), findings are as follows.

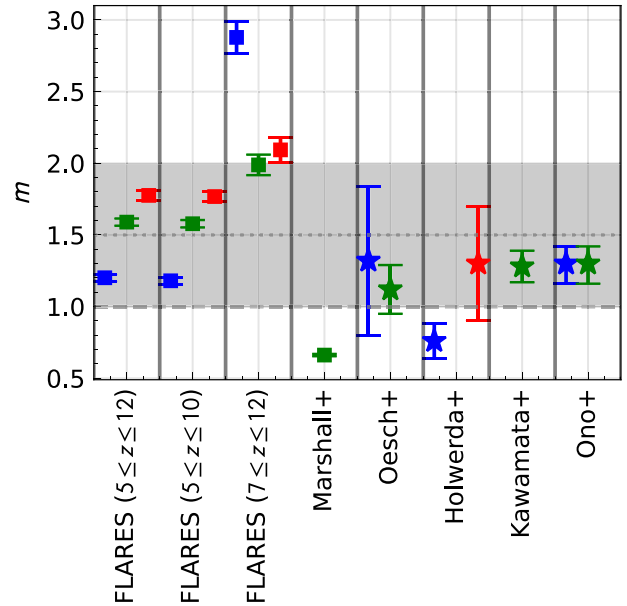


**Figure 13.** A comparison to the slopes of the redshift size evolution derived from observations (Oesch et al. 2010; Ono et al. 2013; Holwerda et al. 2015; Kawamata et al. 2018), and the BLUE TIDES simulation (Marshall et al. 2022). Observations are denoted by stars and simulations are denoted by squares. The shaded range shows the range of slopes found in the FIRE-2 simulations (Ma et al. 2018) for various fixed mass and luminosity galaxy samples. The dashed line corresponds to  $m = 1$ , the theoretical scaling for systems of fixed mass (e.g. Bouwens et al. 2004), and the dotted line corresponds to  $m = 1.5$ , the theoretical scaling for systems with fixed circular velocity (e.g. Ferguson et al. 2004; Hathi et al. 2008). As with Fig. 12, blue points represent a low-luminosity sample ( $L < 0.3 L_{z=3}^*$ ), green points represent an intermediate-luminosity sample ( $0.3 L_{z=3}^* < L < L_{z=3}^*$ ), and red points represent a bright galaxy sample ( $0.3 L_{z=3}^* < L$ ).

(i) The intrinsic size–luminosity relation is bimodal, with one intrinsically compact and bright population and one intrinsically diffuse and dim population.

(ii) These two populations result in a negative slope to the rest-frame far-UV intrinsic size–luminosity distribution.

(iii) Including the effects of dust attenuation results in the perceived size of galaxies to increase, with the most intrinsically compact galaxies increase in size by as much as 50 times.

(iv) The increase in size due to dust attenuation inverts the slope of the size–luminosity relation, resulting in a fair agreement between observations and in this work. However, the FLARES sample lacks low-luminosity compact galaxies that have been shown to steepen the size–luminosity relation in lensing studies. Conversely, the observational samples lack the diffuse and dim galaxies that are present in this work, these act to flatten the size–luminosity relation. The effects of these missing galaxies highlight the need for high-resolution simulations in the future and observationally motivated measurement methods.

(v) Dust distributions in these compact galaxies are highly concentrated with half-metal radii of  $< 1 \text{ pkpc}$ , heavily attenuating the intrinsically bright cores and increasing the observed half-light radius. This may be observable as strong dust gradients.

We performed size measurements for a range of rest-frame UV and visual bands, finding an anticorrelation between the slope of the size–luminosity relation and wavelength. This anticorrelation becomes weaker with decreasing redshift as the intrinsic stellar distribution

increases in size. This represents a falsifiable prediction that the *JWST* will be able to probe at high resolution with NIRC*am*.

We then investigated the evolution of size with redshift in the far-UV, finding slopes for multiple definitions in the range  $m = 1.21$ – $1.87$ . These values are consistent with theoretical predictions modified by additional contributions to the evolution by feedback mechanisms. At low luminosity the evolution is consistent with an evolution at fixed mass ( $m = 1$ ) with additional evolution due to feedback, while high-luminosity galaxies are consistent with a fixed circular velocity evolution ( $m = 1.5$ ), again with an additional contribution from feedback. With the exception of the low-luminosity sample giving a good agreement, these results are in tension with observations. They do however broadly agree with the range found in the FIRE-2 simulations. The limited observational galaxy sample at extremely high redshifts could contribute to this tension. Limiting the galaxy sample to both a low ( $5 \leq z \leq 10$ ) and high ( $7 \leq z \leq 12$ ) redshift sample yielded little change in the results for the low-redshift sample but resulted in significantly higher slopes for the high-redshift sample. This implies a non-constant size evolution with faster evolution in the highest redshift bins. Further observations from future high-redshifts surveys are needed to probe the differences highlighted here in addition to future simulations adding to the theory.

With the launch of the *JWST* we will soon be able to probe these high-redshift regimes with far greater fidelity and further strengthen our understanding of the earliest epochs of galaxy evolution. The *JWST* will allow us to probe higher redshifts at high resolution with NIRC*am*. Not only will this further populate galaxy samples at  $z > 8$ , it will also increase the completeness of the high-redshift observational surveys at low luminosity.

Future work will include the next generation of FLARES simulating a wider range of environments, probing more regions, and simulating a significant volume at high mass resolution. Including higher resolution simulations will enable comparison to the dim and compact galaxies found in lensing studies, while increasing the effective volume with more resimulated regions will allow FLARES to reach a volume comparable to the largest upcoming observational surveys from *Euclid*.

In addition to the next generation of FLARES, the underlying physical processes governing the size evolution in the subgrid model will be probed. This will include stellar and AGN feedback, star formation conditions, and chemical enrichment. The effects of simulation and observational structure detection methods will be investigated to quantify the effect of survey depth and the segmentation of substructures. In particular this will aim to probe the effects of structure detection methods on the diffuse galaxy population and the effect this has on the size–luminosity relation.

## ACKNOWLEDGEMENTS

We thank the EAGLE team for their efforts in developing the EAGLE simulation code.

We acknowledge the indispensable contribution from the publicly available programming language PYTHON (van Rossum 1995), including the NUMPY (Harris et al. 2020), ASTROPY (Astropy Collaboration et al. 2013), MATPLOTLIB (Hunter 2007), SCIPY (Virtanen et al. 2020), and H5PY (Collette 2013) packages.

This work used the DiRAC@Durham facility managed by the Institute for Computational Cosmology on behalf of the STFC DiRAC HPC Facility ([www.dirac.ac.uk](http://www.dirac.ac.uk)). The equipment was funded by BEIS capital funding via STFC capital grants ST/K00042X/1, ST/P002293/1, ST/R002371/1, and ST/S002502/1, Durham Univer-

sity, and STFC operations grant ST/R000832/1. DiRAC is part of the National e-Infrastructure.

CCL acknowledges support from the Royal Society under grant RGF/EA/181016. DI acknowledges support by the European Research Council via ERC Consolidator Grant KETJU (no. 818930). The Cosmic Dawn Center (DAWN) is funded by the Danish National Research Foundation under grant no. 140. MAM acknowledges the support of a National Research Council Canada Plaskett Fellowship, and the Australian Research Council Centre of Excellence for All Sky Astrophysics in 3 Dimensions (ASTRO 3D), through project number CE170100013.

## DATA AVAILABILITY

The integrated galaxy properties used to generate the plots in this paper are available at [flaresimulations.github.io/data](https://flaresimulations.github.io/data). More detailed data, including particle data, can be provided upon request. All the code used to produce the analysis in this paper is public and available at [github.com/WillJRoper/flares-sizes-obs](https://github.com/WillJRoper/flares-sizes-obs).

## REFERENCES

- Astropy Collaboration et al., 2013, *A&A*, 558, A33  
 Barnes D. J., Kay S. T., Henson M. A., McCarthy I. G., Schaye J., Jenkins A., 2017a, *MNRAS*, 465, 213  
 Barnes D. J. et al., 2017b, *MNRAS*, 471, 1088  
 Booth C. M., Schaye J., 2009, *MNRAS*, 398, 53  
 Borrow J., Schaller M., Bower R. G., Schaye J., 2022, *MNRAS*, 511, 2367  
 Bouwens R. J., Illingworth G. D., Blakeslee J. P., Broadhurst T. J., Franx M., 2004, *ApJ*, 611, L1  
 Bouwens R. J. et al., 2015, *ApJ*, 803, 34  
 Bouwens R. J., Illingworth G. D., van Dokkum P. G., Oesch P. A., Stefanon M., Ribeiro B., 2022, *ApJ*, 927, 81  
 Bowler R. A. A., Dunlop J. S., McLure R. J., McLeod D. J., 2017, *MNRAS*, 466, 3612  
 Bowler R. A. A., Cullen F., McLure R. J., Dunlop J. S., Avison A., 2022, *MNRAS*, 510, 5088  
 Bradač M., Schneider P., Lombardi M., Erben T., 2005, *A&A*, 437, 39  
 Bridge J. S. et al., 2019, *ApJ*, 882, 42  
 Calvi V. et al., 2016, *ApJ*, 817, 120  
 Chabrier G., 2003, *PASP*, 115, 763  
 Charlot S., Fall S. M., 2000, *ApJ*, 539, 718  
 Chiang Y.-K., Overzier R., Gebhardt K., 2013, *ApJ*, 779, 127  
 Collette A., 2013, Python and HDF5: Unlocking Scientific Data. O'Reilly Media, Sebastopol, CA  
 Conselice C. J., 2014, *ARA&A*, 52, 291  
 Crain R. A. et al., 2015, *MNRAS*, 450, 1937  
 Cullen L., Dehnen W., 2010, *MNRAS*, 408, 669  
 Dalla Vecchia C., Schaye J., 2012, *MNRAS*, 426, 140  
 Davé R., Anglés-Alcázar D., Narayanan D., Li Q., Rafieferantsoa M. H., Appleby S., 2019, *MNRAS*, 486, 2827  
 Davis M., Efstathiou G., Frenk C. S., White S. D. M., 1985, *ApJ*, 292, 371  
 Dehnen W., Aly H., 2012, *MNRAS*, 425, 1068  
 Dolag K., Borgani S., Murante G., Springel V., 2009, *MNRAS*, 399, 497  
 Feng Y., Di-Matteo T., Croft R. A., Bird S., Battaglia N., Wilkins S., 2016, *MNRAS*, 455, 2778  
 Ferguson H. C. et al., 2004, *ApJ*, 600, L107  
 Ferland G. J. et al., 2017, *Rev. Mex. Astron. Astrofis.*, 53, 385  
 Furlong M. et al., 2015, *MNRAS*, 450, 4486  
 Furlong M. et al., 2017, *MNRAS*, 465, 722  
 Grazian A. et al., 2011, *A&A*, 532, A33  
 Grazian A. et al., 2012, *A&A*, 547, A51  
 Gutkin J., Charlot S., Bruzual G., 2016, *MNRAS*, 462, 1757

- Harris C. R. et al., 2020, *Nature*, 585, 357
- Hathi N. P., Malhotra S., Rhoads J. E., 2008, *ApJ*, 673, 686
- Holwerda B. W., Bouwens R., Oesch P., Smit R., Illingworth G., Labbe I., 2015, *ApJ*, 808, 6
- Holwerda B. W., Bridge J. S., Steele R. L., Kusmic S., Bradley L., Livermore R., Bernard S., Jacques A., 2020, American Astronomical Society, 160, 154
- Hopkins P. F., 2013, *MNRAS*, 428, 2840
- Huang K.-H., Ferguson H. C., Ravindranath S., Su J., 2013, *ApJ*, 765, 68
- Hunter J. D., 2007, *Comput. Sci. Eng.*, 9, 90
- Jiang L. et al., 2013, *ApJ*, 773, 153
- Kawamata R., Ishigaki M., Shimasaku K., Oguri M., Ouchi M., 2015, *ApJ*, 804, 103
- Kawamata R., Ishigaki M., Shimasaku K., Oguri M., Ouchi M., Tanigawa S., 2018, *ApJ*, 855, 4
- Kawinwanichakij L. et al., 2021, *ApJ*, 921, 38
- Kelvin L. S. et al., 2012, *MNRAS*, 421, 1007
- Kennedy R. et al., 2015, *MNRAS*, 454, 806
- La Barbera F., de Carvalho R. R., de la Rosa I. G., Lopes P. A. A., Kohl-Moreira J. L., Capelato H. V., 2010, *MNRAS*, 408, 1313
- Lagos C. d. P. et al., 2015, *MNRAS*, 452, 3815
- Lang P. et al., 2014, *ApJ*, 788, 11
- Laporte N. et al., 2016, *ApJ*, 820, 98
- Liu C., Mutch S. J., Poole G. B., Angel P. W., Duffy A. R., Geil P. M., Mesinger A., Wyithe J. S. B., 2016, *MNRAS*, 465, 3134
- Lovell C. C., Thomas P. A., Wilkins S. M., 2018, *MNRAS*, 474, 4612
- Lovell C. C., Vijayan A. P., Thomas P. A., Wilkins S. M., Barnes D. J., Irodotou D., Roper W., 2021, *MNRAS*, 500, 2127
- Ma X. et al., 2018, *MNRAS*, 477, 219
- McAlpine S. et al., 2016, *Astron. Comput.*, 15, 72
- Marshall M. A., Mutch S. J., Qin Y., Poole G. B., Wyithe J. S. B., 2019, *MNRAS*, 488, 1941
- Marshall M. A., Wilkins S., Di Matteo T., Roper W. J., Vijayan A. P., Ni Y., Feng Y., Croft R. A. C., 2022, *MNRAS*, 511, 5475
- Morishita T. et al., 2018, *ApJ*, 867, 150
- Mosleh M. et al., 2012, *ApJ*, 756, L12
- Mosleh M., Hosseinnejad S., Hosseini-ShahiSavandi S. Z., Tacchella S., 2020, *ApJ*, 905, 170
- Neufeld C. et al., 2021, preprint ([arXiv:2111.14882](https://arxiv.org/abs/2111.14882))
- Oesch P. A. et al., 2010, *ApJ*, 709, L21
- Ono Y. et al., 2013, *ApJ*, 777, 155
- Petrosian V., 1976, *ApJ*, 210, L53
- Planck Collaboration I, 2014, *A&A*, 571, A1
- Popping G. et al., 2022, *MNRAS*, 510, 3321
- Price D. J., 2008, *J. Comput. Phys.*, 227, 10040
- Ribeiro B. et al., 2016, *A&A*, 593, A22
- Rosas-Guevara Y. M. et al., 2015, *MNRAS*, 454, 1038
- Schaller M., Dalla Vecchia C., Schaye J., Bower R. G., Theuns T., Crain R. A., Furlong M., McCarthy I. G., 2015, *MNRAS*, 454, 2277
- Schaye J., Dalla Vecchia C., 2008, *MNRAS*, 383, 1210
- Schaye J. et al., 2015, *MNRAS*, 446, 521
- Sérsic J. L., 1963, *Bol. Asociacion Argentina Astron.*, 6, 41
- Sérsic J. L., 1968, *Atlas de Galaxias Australes*. Observatorio Astronomico, Cordoba, Argentina
- Shibuya T., Ouchi M., Harikane Y., 2015, *ApJS*, 219, 15
- Springel V., White S. D. M., Tormen G., Kauffmann G., 2001, *MNRAS*, 328, 726
- Springel V., Di Matteo T., Hernquist L., 2005a, *MNRAS*, 361, 776
- Springel V. et al., 2005b, *Nature*, 435, 629
- Stanway E. R., Eldridge J. J., 2018, *MNRAS*, 479, 75
- Steidel C. C., Adelberger K. L., Giavalisco M., Dickinson M., Pettini M., 1999, *ApJ*, 519, 1
- Suess K. A., Kriek M., Price S. H., Barro G., 2019, *ApJ*, 877, 103
- Tacchella S. et al., 2015, *ApJ*, 802, 101
- Torrey P. et al., 2015, *MNRAS*, 447, 2753
- Trayford J. W. et al., 2015, *MNRAS*, 452, 2879
- van der Wel A. et al., 2014, *ApJ*, 788, 28
- van Rossum G., 1995, Python Tutorial, Technical Report CS-R9526. Centrum voor Wiskunde en Informatica (CWI), Amsterdam
- Vijayan A. P., Clay S. J., Thomas P. A., Yates R. M., Wilkins S. M., Henriques B. M., 2019, *MNRAS*, 489, 4072
- Vijayan A. P., Lovell C. C., Wilkins S. M., Thomas P. A., Barnes D. J., Irodotou D., Kuusisto J., Roper W. J., 2021, *MNRAS*, 501, 3289
- Virtanen P. et al., 2020, *Nat. Methods*, 17, 261
- Vulcani B. et al., 2014, *MNRAS*, 441, 1340
- Wendland H., 1995, *Adv. Comput. Math.*, 4, 389
- Wiersma R. P. C., Schaye J., Smith B. D., 2009a, *MNRAS*, 393, 99
- Wiersma R. P. C., Schaye J., Theuns T., Dalla Vecchia C., Tornatore L., 2009b, *MNRAS*, 399, 574
- Wilkins S. M., Feng Y., Di-Matteo T., Croft R., Stanway E. R., Bunker A., Waters D., Lovell C., 2016, *MNRAS*, 460, 3170
- Wilkins S. M., Feng Y., Di Matteo T., Croft R., Lovell C. C., Waters D., 2017, *MNRAS*, 469, 2517
- Wilkins S. M., Feng Y., Di Matteo T., Croft R., Lovell C. C., Thomas P., 2018, *MNRAS*, 473, 5363
- Wilkins S. M. et al., 2020, *MNRAS*, 493, 6079
- Wu X., Davé R., Tacchella S., Lotz J., 2020, *MNRAS*, 494, 5636
- Wyithe J. S. B., Loeb A., 2011, *MNRAS*, 413, L38
- Yang L. et al., 2022, preprint ([arXiv:2201.08858](https://arxiv.org/abs/2201.08858))
- Zhang Y.-C., Yang X.-H., 2019, *Res. Astron. Astrophys.*, 19, 006

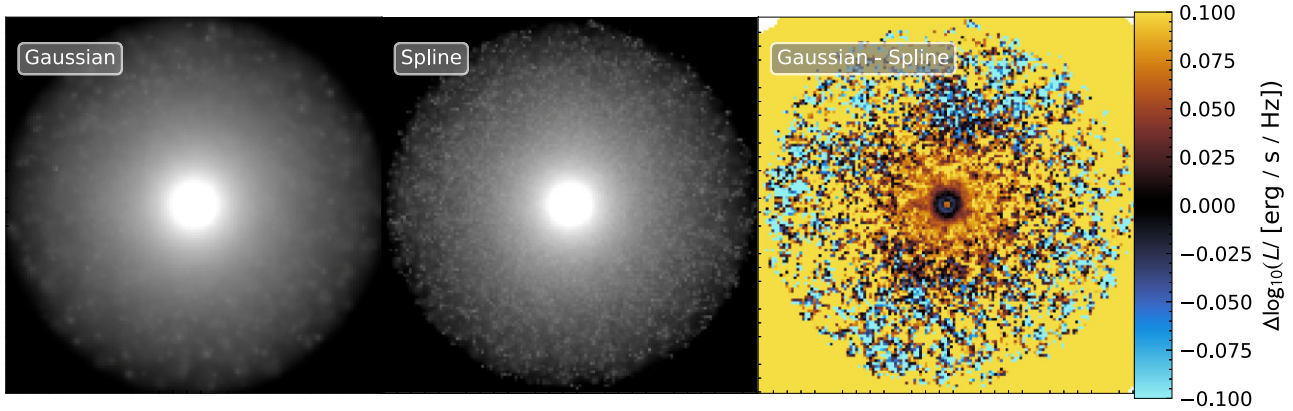
## APPENDIX A: THE EFFECTS OF SMOOTHING

Here we present comparisons between smoothing methods used in image creation first comparing Gaussian and spline kernel smoothing and then the differences between smoothing and ignoring smoothing.

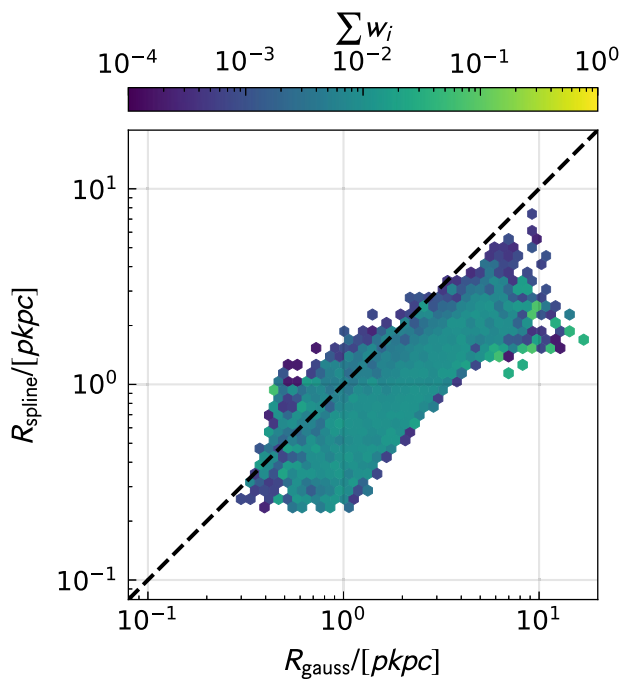
### A1 Comparing kernel averaging to Gaussian smoothing

Fig. A1 shows a comparison between the Gaussian and spline smoothing methods. Qualitatively it can be seen the Gaussian method results in a smoother light distribution due to the indefinite boundaries of the Gaussian smoothing kernel, this spreads light beyond the ‘extent’ given by the SPH kernel. The spline method produces a more granular image with clearer small structures at the outskirts of the FoV. The residual image shows that the Gaussian method’s spreading of light leads to differences at large radii where the Gaussian image is brighter due to the spreading of light. However, this does not mean the Gaussian image is consistently more luminous at large radii, compact structures at large radii in the spline image have more concentrated emission causing these regions to outshine the Gaussian image. This effect is also noticeable in the centre of the image where there is a ring of spline dominated pixels due to this concentration of light. These effects are however minimal with each image differing at most by 0.1 dex.

We further show the effects of smoothing method in Fig. A2 where we compare the measured sizes of galaxies in each method. In the vast majority of cases the Gaussian smoothing results in a larger perceived size due to the increased spread of a single stellar particle’s luminosity. The instances where the spline method yields larger sizes are dominated by smaller galaxies where the dilution of the Gaussian method causes structures to occupy more pixels relative to the more concentrated spline method and thus a larger area is used in the pixel-driven size calculation. It should be noted here that the spline method produces a better agreement with observations with the Gaussian method producing size–luminosity relations that overestimate galaxy sizes relative to observations.



**Figure A1.** A comparison of log-scaled stacked images produced using the Gaussian smoothing method (left), spline kernel method (middle), and a residual image showing the difference between the log of the two methods images. The images themselves are stacks in the far-UV of all galaxies in the FLARES sample (irrespective of completeness).



**Figure A2.** A comparison between the sizes of galaxies measured using the pixel method from the spline (y-axis) and Gaussian (x-axis) smoothing methods. The dashed line represents a 1:1 relation. In this plot we do not differentiate between the compact and diffuse galaxy populations and only present the full complete sample.

### A2 Smoothing versus no smoothing

In Fig. A3, we compare the spline smoothing method to galaxy sizes measured from images where no smoothing has been performed on the stellar particles. In some cases there is minimal difference between the smoothed and unsmoothed measurements, particularly for compact galaxies where the stellar kernels themselves are very small resulting in minimal smoothing. In the vast majority of cases the smoothing increases the measured size, with the most diffuse

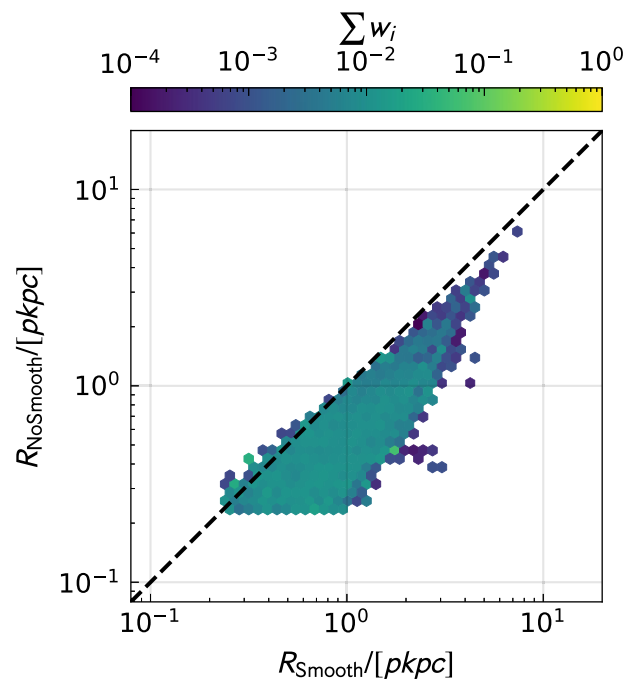


**Figure A3.** A comparison between sizes of galaxies measured using the pixel method from dust attenuated images with and without smoothing of the stellar particles. The dashed line represents a 1:1 relation. In this plot we do not differentiate between the compact and diffuse galaxy populations and only present the full complete sample.

incomplete galaxies (transparent distribution) extending to much larger sizes when smoothed.

## APPENDIX B: SIZE-LUMINOSITY RELATION WAVELENGTH VARIATION

In this appendix, we present the fitting parameters for the wavelength evolution of the size-luminosity relation shown in Fig. 11 (Tables B1 and B2).

**Table B1.** The fitting results for equation (1) for  $z = 7-9$  and all rest-frame bands in Fig. 11.  $R_0$  is a normalization factor,  $\beta$  is the slope of the size–luminosity relation, and  $N$  is the number of galaxies used in each fit.

Redshift ( $z$ ) Band	9		8		7	
	$R_0$	$\beta$	$R_0$	$\beta$	$R_0$	$\beta$
FUV	$0.793 \pm 0.019$	$0.519 \pm 0.026$	$0.842 \pm 0.012$	$0.319 \pm 0.013$	$1.126 \pm 0.011$	$0.290 \pm 0.008$
MUV	$0.773 \pm 0.020$	$0.493 \pm 0.026$	$0.821 \pm 0.012$	$0.313 \pm 0.013$	$1.070 \pm 0.011$	$0.263 \pm 0.008$
NUV	$0.777 \pm 0.021$	$0.485 \pm 0.026$	$0.813 \pm 0.013$	$0.296 \pm 0.014$	$1.020 \pm 0.013$	$0.211 \pm 0.009$
<i>U</i>	$0.687 \pm 0.017$	$0.434 \pm 0.026$	$0.743 \pm 0.011$	$0.262 \pm 0.014$	$0.878 \pm 0.011$	$0.092 \pm 0.010$
<i>B</i>	$0.660 \pm 0.014$	$0.428 \pm 0.025$	$0.704 \pm 0.010$	$0.133 \pm 0.014$	$0.854 \pm 0.010$	$-0.017 \pm 0.010$
<i>V</i>	$0.702 \pm 0.018$	$0.375 \pm 0.024$	$0.689 \pm 0.013$	$0.022 \pm 0.014$	$0.823 \pm 0.011$	$-0.114 \pm 0.009$
<i>R</i>	$0.573 \pm 0.011$	$0.397 \pm 0.027$	$0.638 \pm 0.008$	$0.154 \pm 0.014$	$0.765 \pm 0.009$	$-0.030 \pm 0.011$
<i>I</i>	$0.598 \pm 0.019$	$0.178 \pm 0.026$	$0.601 \pm 0.013$	$-0.110 \pm 0.015$	$0.763 \pm 0.011$	$-0.167 \pm 0.009$
<i>Z</i>	$0.558 \pm 0.015$	$0.229 \pm 0.027$	$0.583 \pm 0.011$	$-0.077 \pm 0.015$	$0.715 \pm 0.010$	$-0.186 \pm 0.010$
<i>Y</i>	$0.595 \pm 0.014$	$0.312 \pm 0.026$	$0.616 \pm 0.010$	$-0.000 \pm 0.014$	$0.715 \pm 0.010$	$-0.183 \pm 0.010$
<i>J</i>	$0.532 \pm 0.017$	$0.090 \pm 0.027$	$0.525 \pm 0.011$	$-0.220 \pm 0.015$	$0.698 \pm 0.010$	$-0.228 \pm 0.009$
<i>H</i>	$0.476 \pm 0.017$	$-0.035 \pm 0.027$	$0.503 \pm 0.011$	$-0.268 \pm 0.014$	$0.688 \pm 0.010$	$-0.250 \pm 0.008$

**Table B2.** The fitting results for equation (1) for  $z = 6-5$  and all rest-frame bands in Fig. 11.  $R_0$  is a normalization factor,  $\beta$  is the slope of the size–luminosity relation, and  $N$  is the number of galaxies used in each fit.

Redshift ( $z$ ) Band	6		5	
	$R_0$	$\beta$	$R_0$	$\beta$
FUV	$1.370 \pm 0.007$	$0.279 \pm 0.004$	$1.692 \pm 0.006$	$0.300 \pm 0.003$
MUV	$1.326 \pm 0.007$	$0.256 \pm 0.004$	$1.639 \pm 0.006$	$0.280 \pm 0.003$
NUV	$1.315 \pm 0.008$	$0.238 \pm 0.004$	$1.627 \pm 0.006$	$0.261 \pm 0.003$
<i>U</i>	$1.218 \pm 0.007$	$0.184 \pm 0.004$	$1.514 \pm 0.006$	$0.215 \pm 0.003$
<i>B</i>	$1.227 \pm 0.007$	$0.111 \pm 0.004$	$1.526 \pm 0.005$	$0.149 \pm 0.003$
<i>V</i>	$1.285 \pm 0.008$	$0.060 \pm 0.004$	$1.604 \pm 0.006$	$0.104 \pm 0.002$
<i>R</i>	$1.106 \pm 0.005$	$0.124 \pm 0.005$	$1.383 \pm 0.004$	$0.156 \pm 0.003$
<i>I</i>	$1.238 \pm 0.008$	$0.021 \pm 0.004$	$1.554 \pm 0.006$	$0.069 \pm 0.002$
<i>Z</i>	$1.155 \pm 0.007$	$0.013 \pm 0.004$	$1.455 \pm 0.005$	$0.064 \pm 0.002$
<i>Y</i>	$1.143 \pm 0.007$	$0.019 \pm 0.004$	$1.439 \pm 0.005$	$0.061 \pm 0.002$
<i>J</i>	$1.161 \pm 0.007$	$-0.023 \pm 0.004$	$1.455 \pm 0.005$	$0.024 \pm 0.002$
<i>H</i>	$1.146 \pm 0.007$	$-0.053 \pm 0.004$	$1.430 \pm 0.005$	$-0.004 \pm 0.002$

## APPENDIX C: THE EFFECTS OF IMAGE RESOLUTION

Image resolution can have a significant effect on measured quantities. In addition to this fact, the resolution one should use to produce synthetic observations from simulations can be unclear, with the softening length often used as a representation of the simulations spatial resolution. We note that the gravity calculations are in fact softened by a factor of  $\sim 2$ , this value indicating a possible larger spatial resolution definition. In Fig. C1, we present a comparison of

sizes derived using the softening length resolution used throughout this paper and a resolution two times worse ( $2 \times s$ ). Our sizes are insensitive to this change producing a clear 1:1 relation with rare pathological instances of large scatter in cases that have little effect on the overall results. This insensitivity is largely due to the fact that many of the structures in galaxies in FLARES already fall below the softening length scale at these redshifts and the measurement methods employ robust interpolation methods to combat resolution effects.

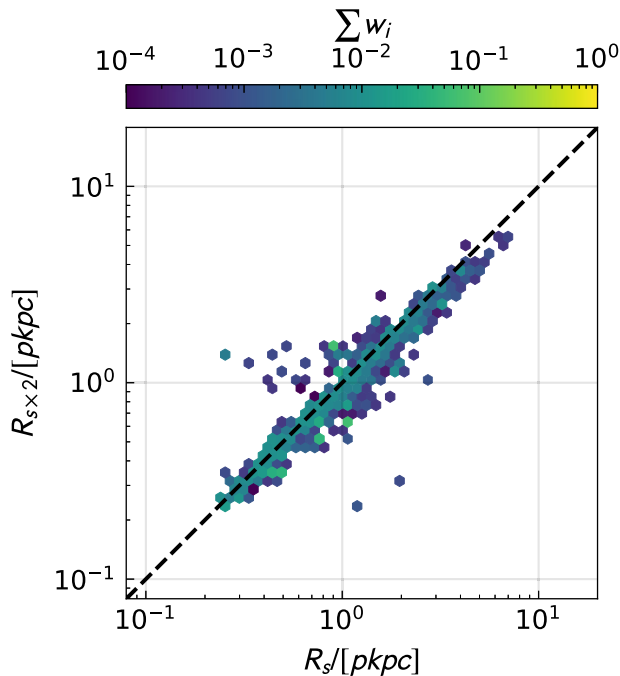


**Figure C1.** A comparison between observed sizes of galaxies using the pixel method at  $z = 5$  measured from images with softening length resolution ( $s = 2.66/(1+z)$  pkpc, x-axis) and images using half that resolution ( $s = 2 \times 2.66/(1+z)$  pkpc, y-axis). The hexbins show the number density weighted using the FLARES weighting scheme. The dashed line represents a 1:1 relation. In this plot we do not differentiate between the compact and diffuse galaxy populations and only present the full complete sample.

#### APPENDIX D: REMOVING BIRTH CLOUD ATTENUATION

Of the parameters used in our synthetic photometry model the birth cloud attenuation is the most uncertain at the epoch investigated in this work. In FLARES II (Vijayan et al. 2021) the values of the photometry model parameters were derived from fits to observational studies and the effects of different values for birth cloud attenuation were probed in Appendix A. For completeness, in Fig. D1, we present a comparison of sizes with and without the birth cloud contribution to attenuation to show its effect on galaxy size.

We can see for the largest (most luminous) galaxies the omission of birth cloud attenuation has little effect on the measured size. These large galaxies have extremely concentrated dust distributions, as shown in Fig. 8, where the attenuation is dominated by the ISM

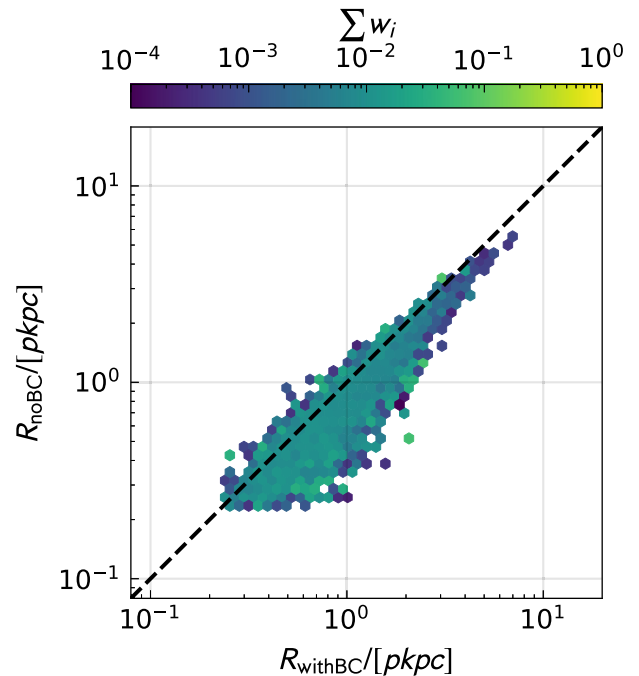


**Figure D1.** A comparison between observed sizes of galaxies using the pixel method at  $z = 5$  measured from photometry including birth cloud attenuation (x-axis) and photometry without the birth cloud contribution (y-axis). The hexbins show the number density weighted using the FLARES weighting scheme. The dashed line represents a 1:1 relation. In this plot we do not differentiate between the compact and diffuse galaxy populations and only present the full complete sample.

contribution. For the smaller (less luminous) galaxies we see a larger scatter in size with a maximum increase of  $\sim 0.5$  dex. These galaxies have a more diffuse dust distribution limiting the contribution to attenuation from the ISM. For galaxies in the diffuse population with young stellar populations the birth cloud attenuation can represent a considerably larger contribution to the overall attenuation. We stress that this comparison is presented to quantify the effect of birth cloud attenuation in the extreme. The model parameters were derived using fits to observational data and thus provide robust results that give a good agreement with observational high-redshift studies not used in the fitting of model parameters.

This paper has been typeset from a  $\text{\TeX}/\text{\LaTeX}$  file prepared by the author.